國 立 交 通 大 學

機 械 工 程 學 系

博 士 論 文

高溫管旋壓縮口分析研究

A Study on Tube Neck-spinning Process at Elevated Temperatures

研 究 生：黃麒禎

指導教授：洪景華　教授

中 華 民 國　一 零 二 年 五 月

高溫管旋壓縮口分析研究

A Study on Tube Neck-spinning Process at Elevated Temperatures

研 究 生：黃麒禎   Student：Chi-Chen Huang

指導教授：洪景華   Advisor：Chinghua Hung

國 立 交 通 大 學

機 械 工 程 學 系

博 士 論 文

A Dissertation

Submitted to Department of Mechanical Engineering

College of Engineering

National Chiao Tung University

in partial Fulfillment of the Requirements

for the Degree of

Doctor of Philosophy

in

Mechanical Engineering

May 2013

Hsinchu, Taiwan

中華民國一零二年五月

高溫管旋壓縮口分析研究

研究生：黃麒禎 　　　　　　　　　　　　　　　　　指導教授：洪景華 教授

國立交通大學機械工程學系

摘要

　　旋壓技術是一種被廣泛運用於製造軸對稱產品之量產方法，本研究將旋壓技術應用於高溫下鋼管瓶口的縮口成型。有限元素分析已成功應用旋壓成型的研究，但目前研究皆在常溫下進行，並未考慮高溫對旋壓縮口的影響。因此，本研究使用有限元素法對於高溫旋壓縮口進行分析研究。

　　為建構一完整的鋼瓶高溫旋壓縮口之有限元素分析模型，本研究首先進行高溫單軸壓縮試驗，且由於材料在高溫下對於應變率相當敏感，因此在不同應變量 (0.05-0.8)、不同溫度 (873-1273 K)與不同應變率 (0.001-50 s^{-1}) 下進行實驗，以獲得較大範圍的材料性質。接著進行鋼瓶高溫旋壓縮口實驗並以商用軟體Abaqus/Explicit針對相同的實驗參數進行有限元素分析，比較實驗與模擬結果在鋼瓶厚度與外形輪廓上的差異。實驗與模擬的誤差在厚度上為8.94%而在外形輪廓上的誤差為1.4%，有限元素模擬結果與實驗有相當的一致性。

　　最後運用驗證過的有限元素模型，研究製程參數對於高溫管旋壓縮口的影響。模擬結果顯示，提高輥輪單位時間的進給量會降低旋壓縮口後的鋼瓶真圓度，並且會增加旋壓縮口製程所需的力量。使用曲線路徑進行旋壓縮口的鋼瓶，其厚度分佈比原始設計的均勻。

關鍵字: 高溫管旋壓縮口、有限元素分析、高溫單軸壓縮試驗、應變率敏感。

A STUDY ON TUBE NECK-SPINNING PROCESS AT ELEVATED TEMPERATURES
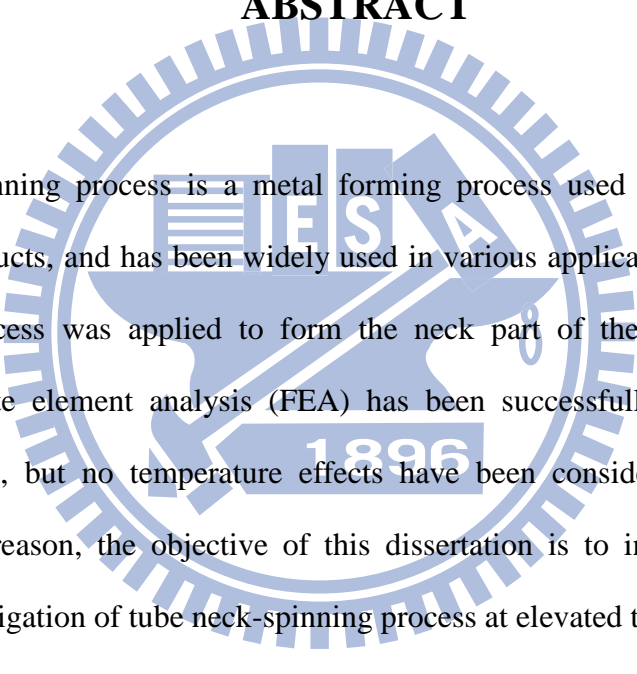
Student: Chi-Chen Huang   Advisor: Prof. Chinghua Hung

Department of Mechanical Engineering
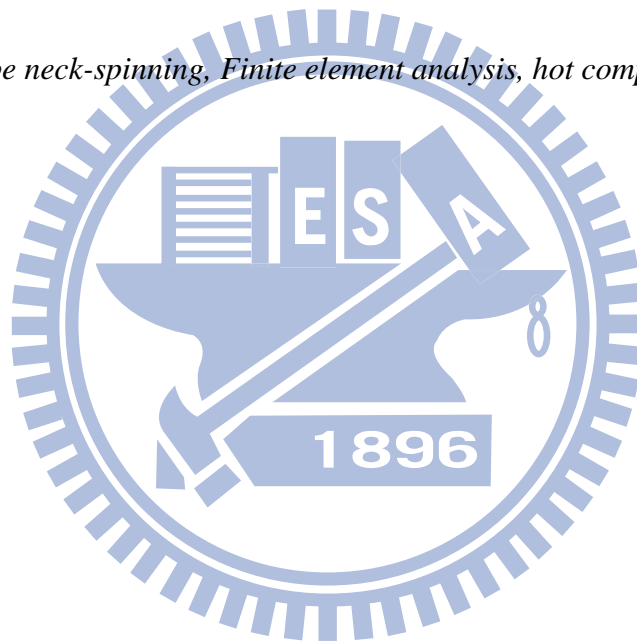
National Chiao Tung University

ABSTRACT

The tube spinning process is a metal forming process used in the manufacture of axisymmetric products, and has been widely used in various applications. In this study, the neck-spinning process was applied to form the neck part of the tube end at elevated temperatures. Finite element analysis (FEA) has been successfully applied to the tube spinning processes, but no temperature effects have been considered on neck-spinning process. For this reason, the objective of this dissertation is to introduce finite element analysis into investigation of tube neck-spinning process at elevated temperatures.

To construct a comprehensive finite element model for tube neck-spinning process at elevated temperatures, this study firstly performed isothermal hot compression tests over a wide range of strain (0.05-0.8), temperatures (873-1273 K), and strain rates (0.001-50 s^{-1}), since the material is sensitive to strain rates at high temperatures. Tube neck-spinning experiments were then performed and the finite element analysis with the same process variables was also conducted by using commercial finite element software, Abaqus/Explicit. Comparisons between experimental and simulation results on thickness distribution and the outer contour of the spun tube were discussed. During the final steps, the average deviations

between the simulation and experiment were 8.94% in thickness and 1.4% in outer contour. The simulation results corresponded well with those derived from the experiment.

Finally, the verified finite element model for tube neck-spinning process at elevated temperatures was used to investigate the influences of two process parameters: the roller feeding pitch and the roller forming path. The roundness of the spun tube became worse and the roller reaction forces increased as the roller feeding pitch increased. For the roller forming path, the thickness distribution of the spun tube formed by curved paths was determined to be more uniform than that of the spun tube formed by straight paths.

Keywords: Hot tube neck-spinning, Finite element analysis, hot compression test, strain rate sensitivity.

誌 謝

<div align="right">黃麒禎　謹誌</div>

TABLE OF CONTENTS

LIST OF TABLES

LIST OF FIGURES

NOMENCLATURE

A_A Material constant in Arrhenius-type model

A_J Yield stress at reference temperature and strain rate in JC model

B_J Coefficient of strain-hardening in JC model

C_J Coefficient of strain rate hardening in JC model

D_i Constant in power equation Y_i

E_i Constant in power equation Y_i

F_i Constant in power equation Y_i

f_s Friction shear stress

m_J Thermal softening exponent

n_A Material constant in Arrhenius-type model

n_J Strain hardening exponent in JC model

p Compressive normal stress

Q Activation energy of deformation

R Universal gas constant

r Correlation coefficient

T Current absolute temperature

T^* Homologous temperature

T_m Melting temperature

T_{ref} Reference temperature

Y_i n_A, Q, and $\ln A_A$

Z Zener-Hollomon parameter

α Material constant in Arrhenius-type model

ε Equivalent plastic strain

$\dot{\epsilon}$ Strain rate

$\dot{\epsilon}^*$ Dimensionless plastic strain rate

$\dot{\epsilon}_0$ Reference strain rate

ϵ Absolute error

μ Coefficient of friction

σ Equivalent flow stress

σ_{exp} Experimental flow stress

$\overline{\sigma}_{exp}$ Mean values of σ_{exp}

σ_p Predicted flow stress

$\overline{\sigma}_p$ Mean values of σ_p
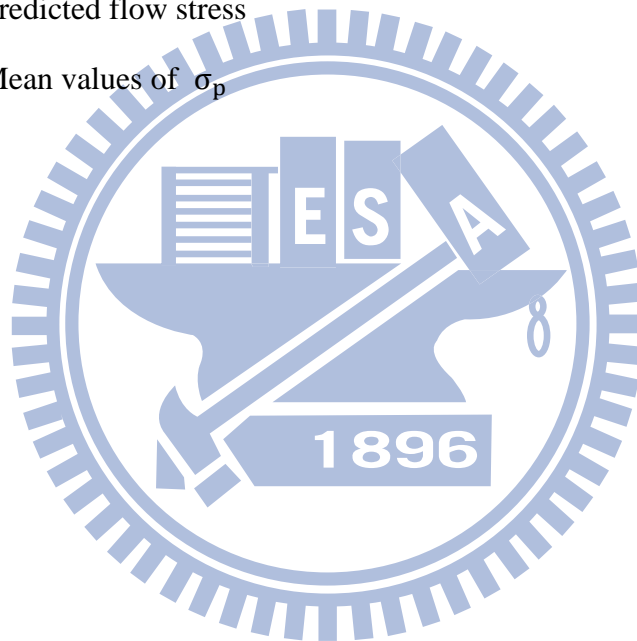
CHAPTER 1 INTRODUCTION

1.1 Introduction

Metal spinning process is a metal forming process used in the manufacture of axisymmetric hollow products. Essentially, all spinning techniques involve rotating a workpiece clamped onto a chuck while the spinning tools approach the workpiece and deform it to the require shape[1]. The spinning process makes it easy to control the dimensions of products. The strength of products also increases during spinning process. Other advantages include a high material usage rate, fewer production stages, a lower forming force, and flexibility in manufacturing. For these reasons, metal spinning process has been widely used in various applications.

The term metal spinning refers to a group of three processes: conventional spinning, shear spinning and tube spinning. A common feature of the three processes is that they allow production of hollow and rotationally symmetric parts. The main difference between the three is apparent in the wall thickness of the workpiece [2]. In conventional spinning, a sheet blank is formed into a desired shape according to the contour of mandrel, and the wall thickness remains constant throughout the process (as shown in Figure 1.1). In contrast, in shear spinning the wall thickness is reduced while the diameter of the part remains constant. A blank of initial thickness t_0 is reduced to a thickness t where the final thickness t is related to the wall angle α by the well known sine law (as shown in Figure 1.2) [2]. In tube spinning, also known as flow forming, a tube is mounted over a rotating mandrel. The roller pressing against the tube advances in the axial direction as the tube rotates under the roller. The wall thickness decreases locally under the pressure of the roller while the roller gradually advances through the tube surface (Figure 1.3). During tube spinning, the thinning of the wall results in elongation of the tube in the axial direction with no change in the nominal diameter [3].
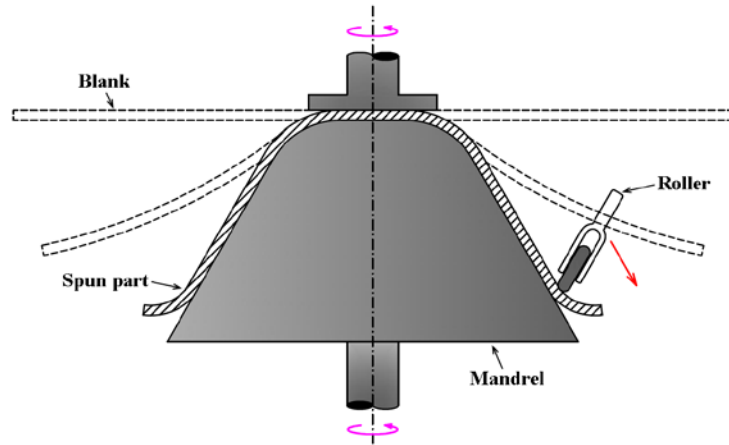
Figure 1.1 Schema of conventional spinning
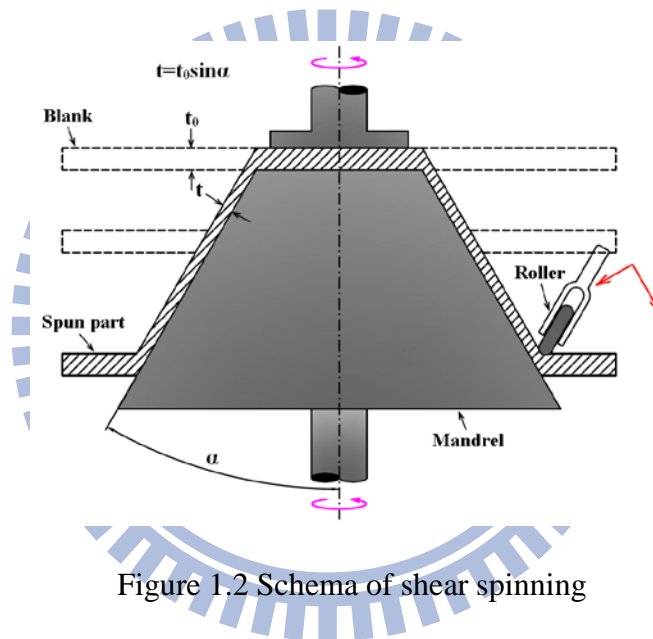
Figure 1.2 Schema of shear spinning
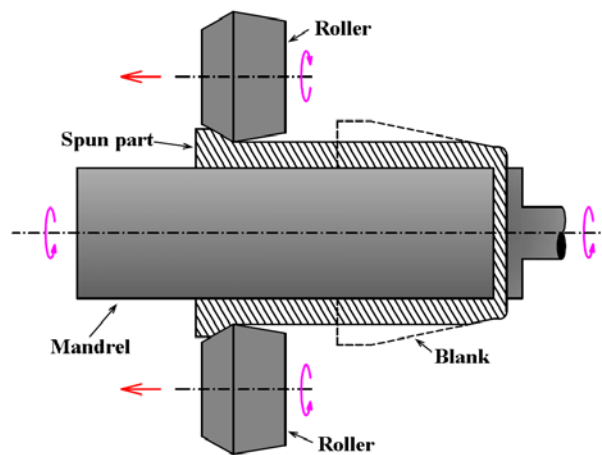
Figure 1.3 Schema of tube spinning

The above-mentioned classification for general spinning processes is widely accepted in literatures; however, in recent years new spinning techniques have appeared. These are not easily classified into conventional spinning, shear spinning and tube spinning, such as neck-spinning, splitting spinning, mandrel-free spinning, asymmetric spinning, etc.

1.2 Neck-spinning Process

Neck-spinning is a kind of spinning process used to reduce the diameter of cylindrical tube ends (as shown in Figure 1.4). In neck-spinning process, rollers displace to form the shape of tube ends. It is usually performed in multiple steps with symmetric rollers. For most applications, mandrel is not necessary during neck-spinning process; therefore, the shape and the wall thickness are controlled by the roller forming path. The mechanics of neck-spinning is quite different from conventional spinning, shear spinning, and tube spinning.
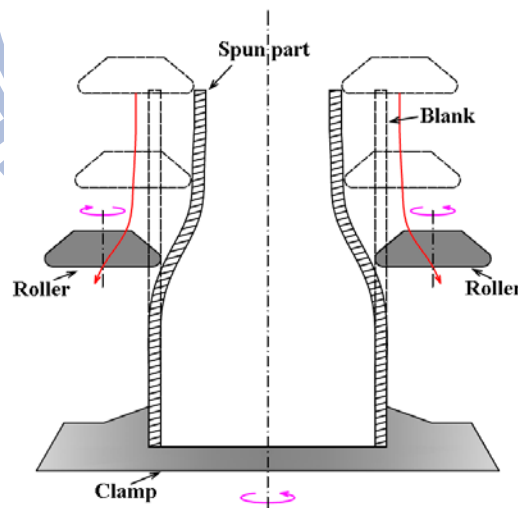
Figure 1.4 Schema of neck-spinning

In this study, the neck-spinning process was applied to form the neck part of high pressure tube ends. High pressure tubes have been widely used in various applications such as gas generants in airbag inflators, motorcycle airbag jackets, compressed gas dusters, soda

3

siphons, and cream whippers. Based on application purposes, various types of gas, such as CO_2, N_2O, N_2, and Ar, are filled in the tubes. This study used a spun tube as a high pressure CO_2 vessel, which is a component of motorcycle airbag jackets.

For this application of neck-spinning, the process should be performed at elevated temperatures. In high pressure vessel, the tube end is formed into domed shape and boss (as shown in Figure 1.5). The reduction of diameter is quite large at the tube end, so performing the neck-spinning process at room will cause a fracture to occur (as shown in Figure 1.6). Therefore, in this study, the neck-spinning of tube should be performed at elevated temperatures to prevent fracture.
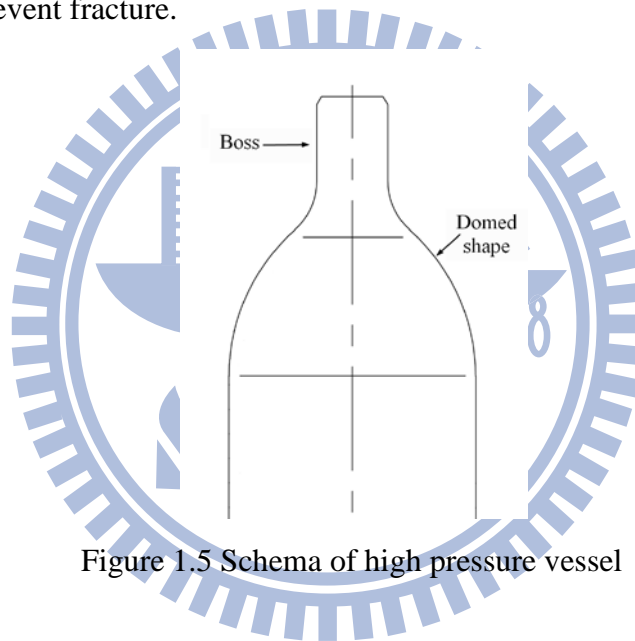
Figure 1.5 Schema of high pressure vessel

Figure 1.6 Facture after spinning at room temperature

1.3 Literature Review

Several researchers have conducted experimental and theoretical investigations on the influence of the various parameters on the spinning process [4]-[11]. Progress in computation capability and software coding has enabled the application of finite element analysis to the tube spinning process. Hauk et al. [12] used an axisymmetric model and a one-thirty sixth 3D model to simulate the flow-splitting process. Only a few steps of flow-splitting were simulated successfully using three-dimensional model due to large computation time and difficulties during manual remeshing; therefore, three-dimensional simulation of flow-splitting process at that time can hardly be applied to determine the proper process parameters. Iguchi et al. [13] used a dynamic-explicit code DYNA-3D to analyze the spinning manufacturing process for exhaust system components of motor vehicles. The results showed the distribution of stress and strain which evolved in the material during spinning. This provided useful information for the prediction of failures during spinning. During spinning, the material temperature increased to as high as 300 ℃; however, changes in temperature and material properties were not considered in their simulation due to the computation cost. Hua et al. [14] used ANSYS to establish a three-dimensional elastic-plastic finite element model for the three-roller backward spinning of a cylindrical workpiece. The simulation results showed a variety of phenomena that occur during spinning. These included bell-mouth distortion, build-up, bulging in the front of and between the rollers, and diametric reduction and growth. Although both experiment and simulation of backward spinning were performed in their paper, the simulated results were not quantitatively verified by experimental data. Xia et al. [15] used MARC to simulate the process of multi-pass offset tube neck-spinning. Their results showed that the distribution of strain and stress was non-axisymmetric; the equivalent stress distributes and varies along the axial direction section by section and reached a maximum at the opening end of the spun workpiece. The thickness reduction at the opening end, and the ellipticity and axial elongation of the spun workpiece increased with increasing spinning passes. The linearity of forward path spinning

was significantly less than that of backward path spinning. Similarly, the simulated results were not quantitatively verified by experimental data.

In the above literature, the tube spinning processes were all performed at room temperature. Figure 1.6 shows that performing the spinning process at room temperature will cause a fracture at the top of the tubes, especially when the deformation is large. However, few studies have mentioned tube spinning at elevated temperatures. Makoto et al. [16] invented a new CNC spinning machine comprised of rollers with heaters. The heated rollers heated the magnesium tubes and formed them into various shapes by spinning. The forming possibility of magnesium tubes was experimentally demonstrated. However, the heated rollers are not suitable to apply to form the material at high temperatures because the rigidity of rollers decreases as the temperature increases. Mori et al. [17] developed a hot shear spinning process of cast aluminum alloy parts to eliminate casting defects and obtain a desired distribution of wall thickness. Hot air heated the blank during the shear spinning process to maintain the forming temperature at 400 ℃. The commercial software LS-DYNA was adopted to simulate the hot shear spinning but only the distribution of equivalent plastic strain was presented and the simulated results did not compare to the experimental data. Yang et al. [18] established a 3D coupled thermo-mechanical FE model of the hot splitting spinning process of magnesium alloy AZ31. The influence of different initial temperatures of the disk blank and different feed rates of the splitting rollers on forming quality of deformed flanges was investigated numerically. However, no experimental data were proposed to verify the simulation results. In summary, finite element analysis has been successfully applied to the tube spinning processes, but no temperature effects have been considered on tube neck-spinning.

1.4 Objective of Present Study

Despite the above-mentioned efforts on introducing FEA into metal spinning process, a complete and accurate finite element model for neck-spinning process at elevated temperatures has not yet been proposed. Therefore, the objective of this study is to construct a comprehensive finite element model to investigate the tube neck-spinning process at elevated temperatures. Comparing the results of the simulation and the experiment would verify the finite element model. Furthermore, the verified finite element model will be used to discuss the influence of the roller feeding pitch and to investigate numerically the roller forming paths to improve the thickness distribution.

1.5 Research Method

In current industrial practice, production of high pressure vessel requires two processes. First, the closed-bottom cylindrical tube is manufactured from sheet steel using multi-stage deep drawing process. Diameter of the tube end is then reduced using neck-spinning process (as shown in Figure 1.7).
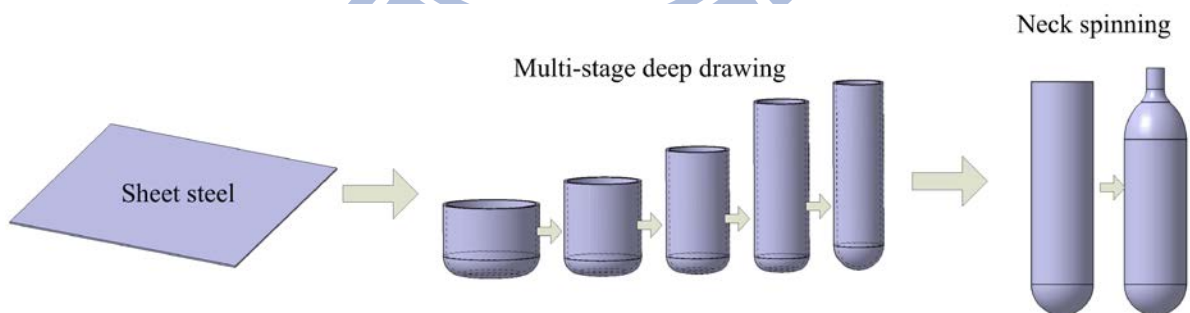
Figure 1.7 Production of high pressure vessel

The deep drawing process is highly efficient for manufacturing closed-bottom tubes, but the tubes manufactured using deep drawing are unsuitable for this study. In finite element analysis on neck-spinning process, accurate material properties of the tubes are important.

However, it is hard to cut specimens from the tube due to its small diameter so that specimens can only be cut from original sheet steel. Hence, the work hardening effect of the deep drawing process will be ignored in the simulation. Moreover, only tensile tests can be conducted using sheet specimens but the internal stress states generated in the material during neck-spinning process are different from those during tensile test. To resolve the above problem, original material was changed from sheet steel to rod steel; therefore, the tubes for neck-spinning and specimens are identically manufactured from rod steel using turning and boring without other work processes, thus compression test can be conducted using rod specimen.

In order to construct an accurate and comprehensive finite element model for neck-spinning process at elevated temperatures, this study firstly performed material tests to obtain properties of the tube. Low carbon rod steel AISI 1020 was used in this study. Uniaxial compression tests were conducted at various temperatures and strain rates since the material is sensitive to strain rates at high temperatures. Neck-spinning experiments were then performed and the finite element analysis with the same process variables was also conducted by commercial finite element software, Abaqus/Explicit, incorporating these obtained material properties. After verifying the consistency of simulated and experimental results, a comprehensive finite element model for neck-spinning process of tubes at elevated temperatures was assured. Finally, the finite element model was used to find the proper process variables and to analyze the influence of roller forming paths on neck-spinning process.

1.6 Structure of Dissertation

This chapter introduces the background and application of the tube neck-spinning process at elevated temperatures. Chapter 2 presents the experiments of material properties and corresponding constitutive models of the flow behavior. Chapter 3 specifies experiments

of neck-spinning process. A finite element analysis of neck-spinning process and comparison between experimental and simulated results are discussed in chapter 4. The influences of process variables and roller forming paths are discussed in chapter 5. Finally, chapter 6 concludes and summaries this study.

CHAPTER 2 MATERIAL PROPERTY EXPERIMENTS

At high temperatures or hot working process, the material properties are sensitive to strain rates. In this case, the strain rate value was as high as $30s^{-1}$ during the hot neck-spinning process. Therefore, the finite element simulation should include the strain rate effect of flow stress.

In order to obtain flow behavior of material for constructing the finite element model for the tube neck-spinning process at elevated temperature, this study performed isothermal hot compression tests in a wide range of temperatures, strain and strain rates. Constitutive models of flow behavior were used to fit the experimental data. Detailed descriptions are presented in the following sections.

2.1 Compression Tests

The material used in this study was low carbon steel AISI 1020, manufactured from China Steel Corporation. The isothermal hot compression tests were performed at three temperatures (873, 1073, and 1273 K) and six strain rates (0.001, 0.01, 0.1, 1, 10, and 50 s^{-1}). The tests under lower strain rates (0.001, 0.01, and 0.1 s^{-1}) were conducted using a thermo-mechanical simulation machine, Gleeble-3500, as Figure 2.1 shows. Cylindrical specimens with 6 mm in diameter and 9 mm in height were used. The high temperature compression tests were conducted in argon atmosphere. Each specimen was heated to a desired temperature at a rate of 10K s^{-1} using direct resistance heating and held for 1 min at isothermal condition before compression tests in order to obtain a steady temperature. The maximum true strain is 0.8.

The tests under higher strain rates (1, 10, and 50 s^{-1}) were carried out on thermo-mechanical simulator, THERMECMASTOR-Z, as Figure 2.2 shows. Cylindrical

specimens with 8 mm in diameter and 12 mm in height were used. The high temperature compression tests were conducted in low vacuum (300-500 Pa). Each specimen was heated to a desired temperature at a rate of 10K s^{-1} using high frequency induction heating and held for 1 min at isothermal condition before compression tests in order to obtain a steady temperature. The maximum true strain is also 0.8.
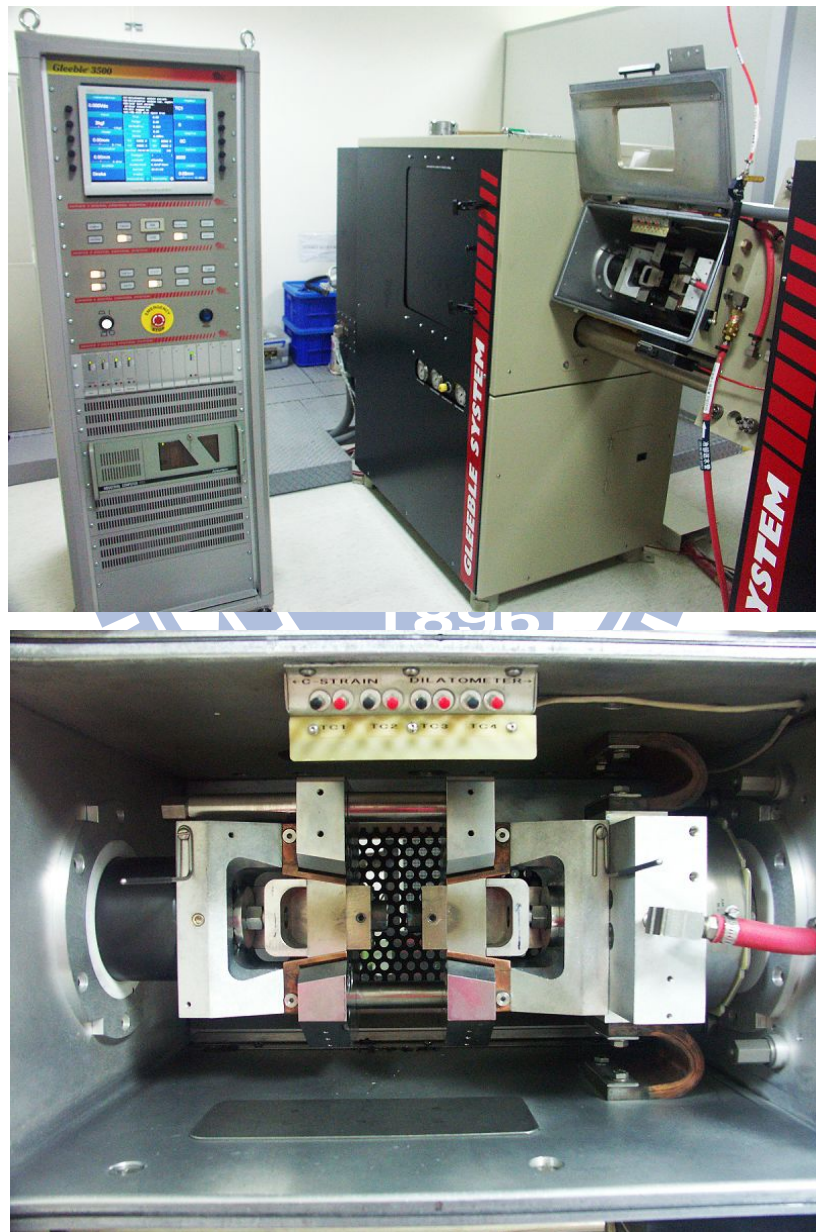
Figure 2.1 Thermo-mechanical simulation machine (Gleeble 3500, Dynamic System Inc.) in

ITRI South
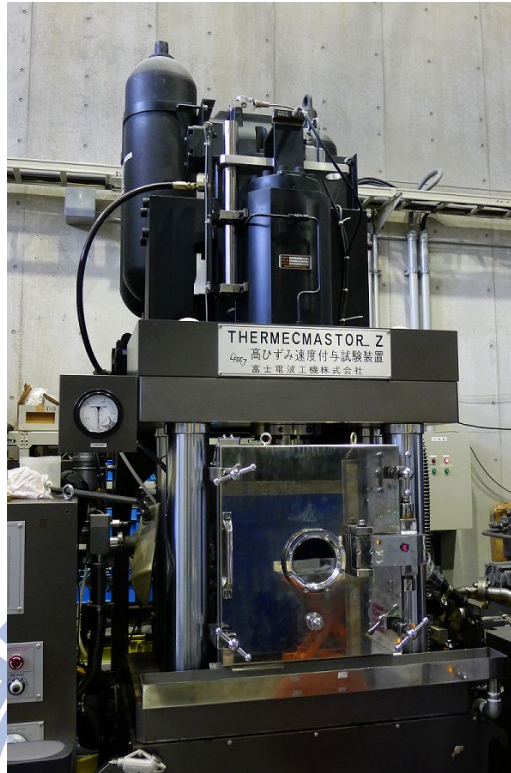
Figure 2.2 Thermo-mechanical simulator (THERMECMASTOR-Z, Fuji Electronic Industrial Co.) in Chair for Hyper-functional Forming, Institute of Industrial Science, The University of Tokyo.

The true stress-strain curves of AISI 1020 steel at various strain rates and the corresponding temperatures were obtained from above uniaxial hot compression tests as shown in Figure 2.3. It can be found that the flow stress changes significantly with respect to strain rate and temperature. The flow stress increases with the increase in strain rate and the decrease in temperature. The flow stress curves present a peak stress at a small strain due to the dominance of work hardening. Then the flow stress decrease, which is related with dynamic recovery, dynamic recrystallization, etc. Finally, the stress becomes steady as a balance between softening and hardening [19][20].
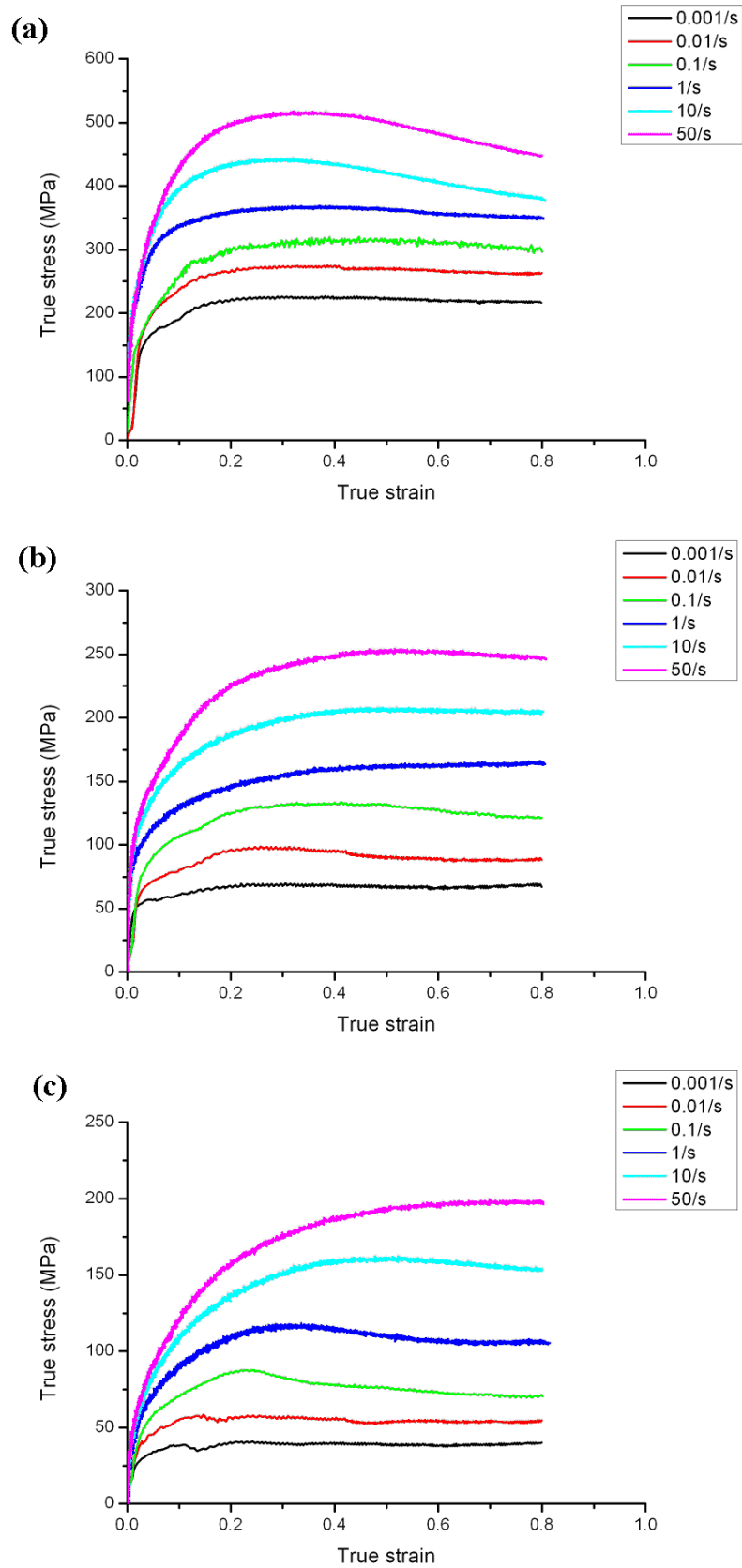
Figure 2.3 True stress-strain curves obtained from hot compression tests of AISI 1020 steel

under various strain rates at temperatures of (a) 873K, (b) 1073K, and (c) 1273K.

2.2 Constitutive Equations of Flow Stress

Material flow behavior is often complex during hot forming process. The hardening and softening mechanisms are both significantly affected by many factors such as strain, strain rate, and temperature [19]. Constitutive equation is the mathematical representation of the flow behavior of materials with respect to affecting factors [21]. The constitutive models may be mainly divided into two groups [19][22]:

(1) *Phenomenological constitutive models*: These models provide a definition of the material flow stress based on empirical observations and comprise some mathematical functions. Phenomenological models lack physical background and just fit for experimental observations. In addition, number of material constants of the models are reduced and easily calibrated.

(2) *Physical-based constitutive models*: These models account for physical aspects of the material behavior. Most of them are derived from the theory of thermodynamics, thermally activated dislocation movement, and kinetic of slips. Compared with phenomenological models, they allow for an accurate definition of material behaviors under wide ranges of loading conditions by using a large number of material constants and some physical assumptions.

Physical-based constitutive models usually provide more accurate representation of the flow behavior of materials; however, these models involve larger number of material constants, which should be obtained from more data of precisely controlled experiments [21]. Therefore, this study used two well-known phenomenological constitutive models, Johnson-Cook and Arrhenius-type constitutive models, to fit the experimental results of AISI 1020 steel at various temperatures and strain rates.

2.2.1 Johnson-Cook (JC) Constitutive Model

Johnson and Cook [23] proposed a constitutive model for metals subjected to large strains, high strain rates, and high temperatures. The JC model has been widely used for a variety of materials at different ranges of temperature and strain rate [21][23][24]. Additionally, the JC model is available in various commercial finite element codes, such as Abaqus and LS-DYNA. The Johnson-Cook model can be expressed as:

$$\sigma = \left(A_J + B_J\varepsilon^{n_J}\right)\left(1 + C_J \ln \dot{\varepsilon}^*\right)(1 - T^{*m_J}) \tag{2.1}$$

where σ is the equivalent flow stress, ε is the equivalent plastic strain, A_J is the yield stress at reference temperature and reference strain rate, B_J is the coefficient of strain-hardening, n_J is the strain hardening exponent, $\dot{\varepsilon}^* = \dot{\varepsilon}/\dot{\varepsilon}_0$ is the dimensionless plastic strain rate ($\dot{\varepsilon}$ is the strain rate, and $\dot{\varepsilon}_0$ is the reference strain rate), and T^* is the homologous temperature and expressed as:

$$T^* = {T - T_{ref}}/{T_m - T_{ref}} \tag{2.2}$$

where T is the current temperature, T_m is the melting temperature (1643 K for AISI 1020 steel), and T_{ref} is the reference temperature ($T \geq T_{ref}$). C_J and m_J are the material constants represented the coefficients of strain rate hardening and thermal softening exponent, respectively.

In equation (2.1), the expression in the first set of brackets represents the strain hardening effect, and the second represents the strain rate sensitivity, and the third set of brackets represents the temperature dependence of stress [25]. The effect of strain, strain rate, and temperature are decoupled in the JC model.

The first step to obtain the material constants of JC model is to reduce equation (2.1) to equation (2.3) at reference temperature, 873 K, and reference strain rate, 1 s^{-1}.

$$\sigma = A_J + B_J\varepsilon^{n_J} \tag{2.3}$$

The value A is calculated from the yield stress at 873 K and 1 s^{-1}. Subtracting A and

taking natural logarithm of both side of equation (2.3) gives:

$$\ln(\sigma - A_J) = n_J \ln \varepsilon + \ln B_J \qquad (2.4)$$
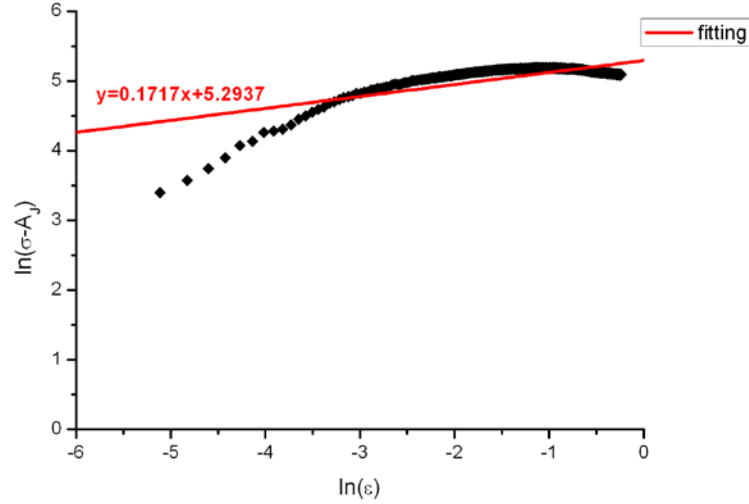
Figure 2.4 Relationships between $\ln(\sigma - A_J)$ and $\ln \varepsilon$ at a temperature of 873 K and a strain rate of 1 s^{-1}

From the $\ln(\sigma - A_J)$ vs. $\ln \varepsilon$ plot (Figure 2.4), n_J and $\ln B_J$ is obtained from the slope and y-intercept of linear fitting line, respectively. At reference temperature, 873 K, the thermal softening term is equal to 1, as $T^* = 0$. The equation (2.1) can be expressed as:

$$\sigma = (A_J + B_J \varepsilon^{n_J})(1 + C_J \ln \dot{\varepsilon}^*) \qquad (2.5)$$

At a particular strain value, e.g. 0.5, C is calculated from the slope of linear fitting line of $\sigma/(A_J + B_J \varepsilon^{n_J})$ vs. $\ln \dot{\varepsilon}^*$ plot (Figure 2.5). Similarly, the procedures were repeated to obtain the values of C_J at various strains over the range 0.05-0.8 at interval 0.05. Figure 2.6 shows the value of C_J at various strain values. Because C_J is independent of strain in JC model, the final C_J is the mean value of C_J obtained at different strain value.
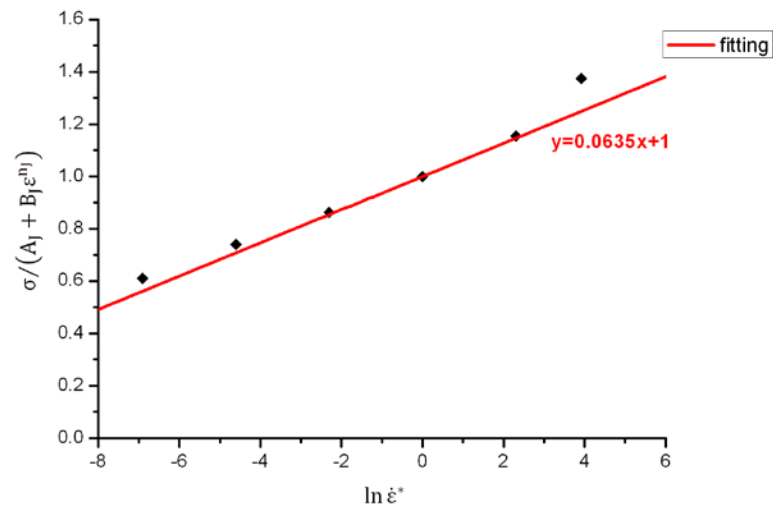
Figure 2.5 Relationships between $\sigma/(A_J + B_J\varepsilon^{n_J})$ and $\ln\dot{\varepsilon}^*$ at a temperature of 873 K and a strain of 0.5
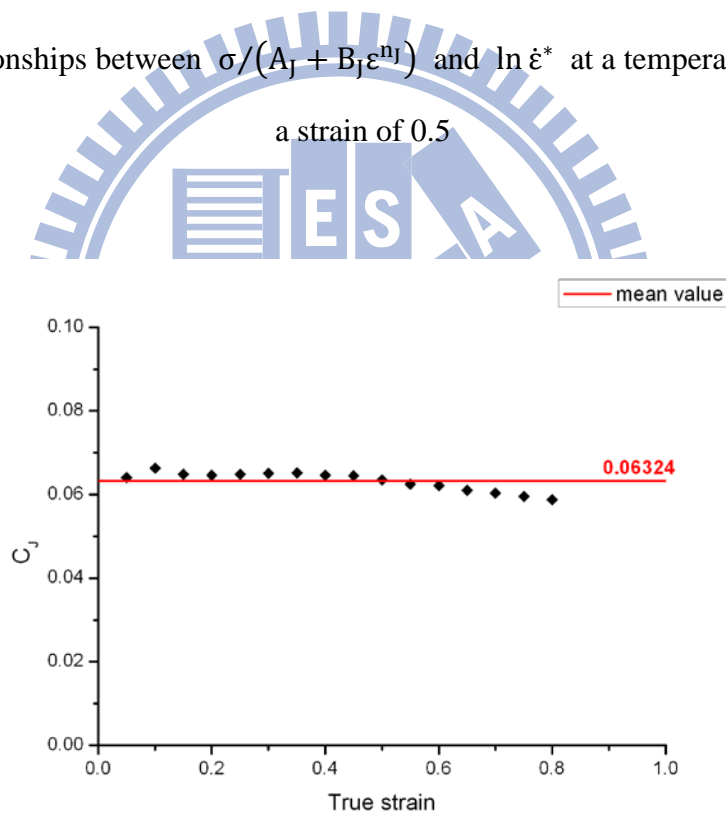
Figure 2.6 The value of parameter C_J in Johnson-Cook constitutive model

At reference strain rate, 1 s^{-1}, the strain rate hardening term is equal to 1, as $\ln\dot{\varepsilon}^* = 0$. So, the equation (2.1) can be expressed as:

$$\sigma = \left(A_J + B_J\varepsilon^{n_J}\right)(1 - T^{*m_J}) \tag{2.6}$$

At a particular strain value, e.g. 0.5, m_J is calculated from the slope of linear fitting line of $\ln\left\{1 - \left[\sigma/\left(A_J + B_J\varepsilon^{n_J}\right)\right]\right\}$ vs. $\ln T^*$ (Figure 2.7). Similar procedures were repeated to obtain the value of m_J at various strains (as shown in Figure 2.8). Because m_J is independent of strain in JC model, the final m_J is the mean value of m obtained at different strain value.
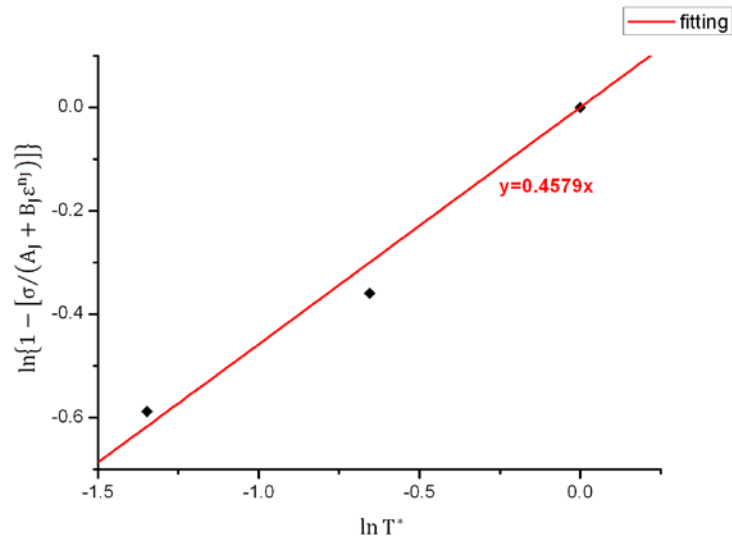
Figure 2.7 Relationships between $\ln\left\{1 - \left[\sigma/\left(A_J + B_J\varepsilon^{n_J}\right)\right]\right\}$ and $\ln T^*$ at a strain rate of 1 s^{-1} and a strain of 0.5
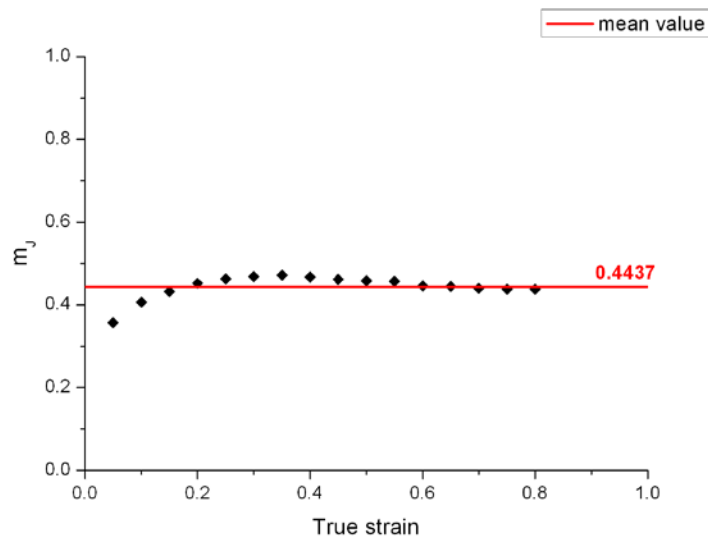
Figure 2.8 The value of parameter m_J in Johnson-Cook constitutive model
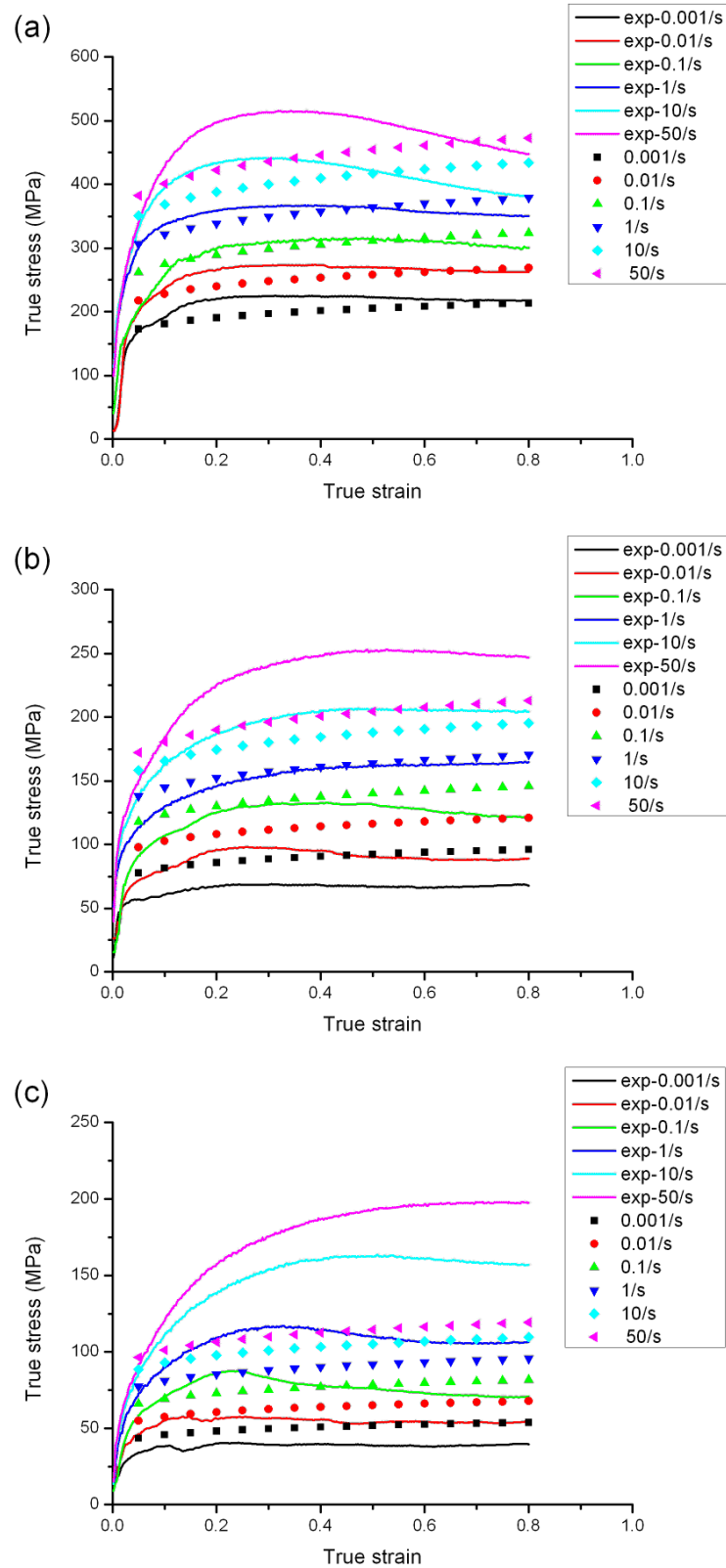
Figure 2.9 Comparison between experimental and predicted flow stress curves using Johnson-Cook constitutive model under various strain rates at temperatures of (a) 873K, (b) 1073K, and (c) 1273K.

Table 2.1 Material constants of Johnson-Cook model for AISI 1020 steel

A_J (MPa)	B_J (MPa)	n_J	C_J	m_J
187.6	199.1	0.1717	0.06324	0.4437

The material constants of the JC model for AISI 1020 steel are listed in Table 2.1, hence the flow stress data can be predicted at variable strains, strain rates, and temperatures. The comparison between experimental and predicted flow stress curves under various strain rates (0.001, 0.01, 0.1, 1, 10, and 50 s^{-1}) and temperatures (873, 1073, and 1273 K) is shown in Figure 2.9. Two estimates are used to evaluate the accuracy of prediction of constitutive model. They are absolute error (ϵ), and correlation coefficient (r). The absolute error can be expressed as:

$$\epsilon = \left| \frac{\sigma_p - \sigma_{exp}}{\sigma_{exp}} \right| \times 100\% \tag{2.7}$$

where σ_p is the predicted flow stress and σ_{exp} is the experimental flow stress.
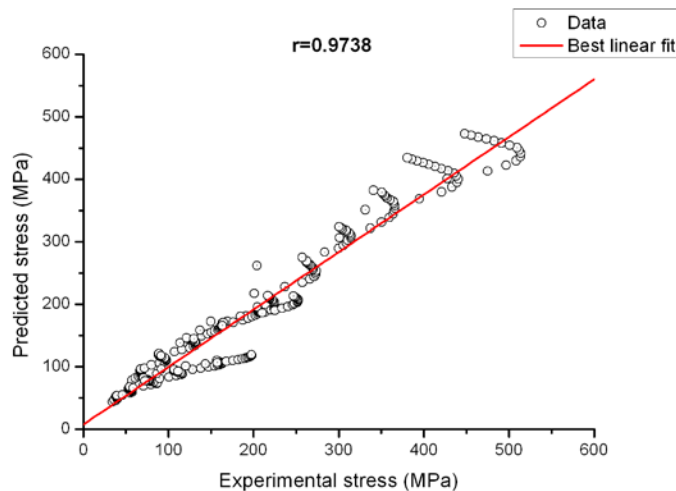
Figure 2.10 Correlation between experimental and predicted flow stress using Johnson-Cook model under range of strain (0.05-0.8 in steps of 0.05), strain rates (0.001-50 s^{-1}), and temperatures (873-1273 K).

The correlation coefficient is commonly used to measure the strength of a linear relationship between two values, and here it can be expressed as:

$$r = \frac{\sum_{i=1}^{N}(\sigma_p^i - \bar{\sigma}_p)(\sigma_{exp}^i - \bar{\sigma}_{exp})}{\sqrt{\sum_{i=1}^{N}(\sigma_p^i - \bar{\sigma}_p)^2 \sum_{i=1}^{N}(\sigma_{exp}^i - \bar{\sigma}_{exp})^2}} \tag{2.8}$$

where $\bar{\sigma}_p$ and $\bar{\sigma}_{exp}$ are the mean values of σ_p and σ_{exp}, respectively.

Figure 2.10 shows the correlation between experimental and predicted flow stress using JC model under range of strain (0.05-0.8 in steps of 0.05), strain rates (0.001-50 s⁻¹), and temperatures (873-1273 K). The correlation coefficient (r) was 0.9738. The correlation between experimental and predicted flow stress was high, but it did not imply that the predictability was accurate.

Figure 2.11 and Table 2.2 show the average absolute errors between experimental and predicted flow stress using JC model under various strain rates (0.001-50 s⁻¹) and temperatures (873-1273 K). The average absolute errors between experimental and predicted flow stress for all condition was 15.27%. The errors of prediction at reference temperature, 873K, were all below 10%, whereas significant errors were observed at the other higher temperature. Furthermore, the errors in the cases under strain rate near the reference strain rate, 1 s⁻¹, were relatively smaller. During the fitting procedure, only partial experimental data, conducted at reference strain rate and temperature, were used so that the predictions at those conditions were accurate. However, in the JC model, five material constants are assumed to be independent of strain, strain rate, and temperature, so the material constants obtained from partial experimental data should be extended to predict all flow stresses under other strain rates and temperatures condition. For the AISI 1020 steel in this study, the assumption is not reasonable because of the significant error of prediction at 1073K and 1273K. In summary, the Johnson-Cook model was not suitable enough for predicting the flow stresses of AISI 1020 steel in this study.
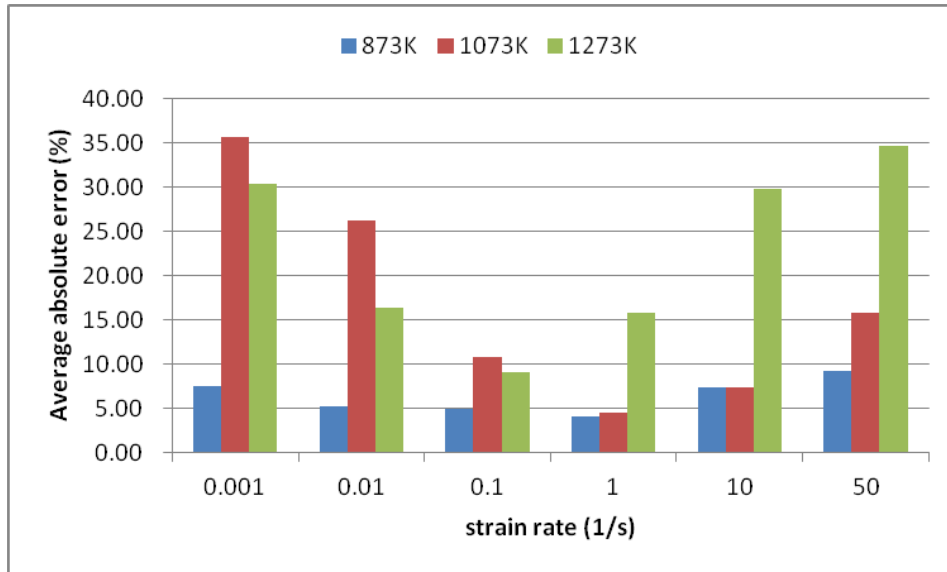
Figure 2.11 Average absolute errors between experimental and predicted flow stress using

J-C model under various strain rates (0.001-50 s^{-1}) and temperatures (873-1273 K).

Table 2.2 Average absolute errors between experimental and predicted flow stress using J-C

constitutive model under strain rates (0.001-50 s^{-1}) and temperatures (873-1273 K) (unit: %)

		Strain rate					
		0.001/s	0.01/s	0.1/s	1/s	10/s	50/s
	873K	7.53	5.29	4.95	4.10	7.42	9.22
Temperature	1073K	35.61	26.23	10.85	4.46	7.45	15.79
	1273K	30.34	16.34	9.03	15.77	29.77	34.69

2.2.2 Arrhenius-type Constitutive Model

Sellar and McTegart [26] proposed a constitutive model expressed in a hyperbolic-sine

Arrhenius-type equation for hot deformation of material including the influence of

temperature and strain rate. The Arrhenius equation is widely used to describe the relationship

between the strain rate, flow stress and temperature, especially at high temperatures [19]. The

Arrhenius-type model can be expressed as:

$$\dot{\varepsilon} = A_A[\sinh(\alpha\sigma)]^{n_A} \exp(-Q/RT) \tag{2.9}$$

where $\dot{\varepsilon}$ is strain rate (s^{-1}); σ is flow stress (MPa); Q is an activation energy of deformation (J mol^{-1}); R is the universal gas constant (8.31 J mol^{-1} K^{-1}); T is the absolute temperature (K); A_A, α, and n_A are parameters independent of temperature.

Equation (2.9) can be conveniently represented in terms of a temperature compensated strain rate parameter [27], the Zener-Hollomon parameter in an exponent-type equation, Z [28]:

$$Z = \dot{\varepsilon}\exp(Q/RT) \tag{2.10}$$

The hyperbolic-sine Arrhenius-type equation was normally used to describe steady state flow stress, but it was found that the equation can be used for any other strains using parameters Q, A_A, α, and n_A as a function of strain[21], [27], [29], [32].

The first step to obtain the material constants of Arrhenius-type constitutive model is to take natural logarithm of both side of equation (2.9):

$$\ln[\sinh(\alpha\sigma)] = \frac{1}{n_A}\ln\dot{\varepsilon} + \frac{Q}{n_A RT} - \frac{1}{n_A}\ln A_A \tag{2.11}$$

Form equation (2.11), the parameter n_A can be calculated from the slope of the linear fitting line of $\ln[\sinh(\alpha\sigma)]$ vs. $\ln\dot{\varepsilon}$ plot at a particular strain value. Furthermore, the fitting line of experimental data under different temperature should be parallel because parameter n_A is independent of temperature. The parameter α is an additional adjustable constant which brings $\alpha\sigma$ into the correct range to make constant T curves in $\ln[\sinh(\alpha\sigma)]$ vs. $\ln\dot{\varepsilon}$ plot linear and parallel [33]. Therefore, an optimization is used to find the value of α to minimize the error between experimental data and linear fitting lines under various temperatures. Figure 2.12 shows the relationships between $\ln[\sinh(\alpha\sigma)]$ and $\ln\dot{\varepsilon}$ at various temperatures and a strain of 0.5 using the optimal value of α. Similarly, the procedures were repeated to obtain the values of α and n_A at various strains over the range 0.05-0.8 at interval 0.05. Figure 2.13 and Figure 2.14 show the values of α and n_A at various strains, respectively.
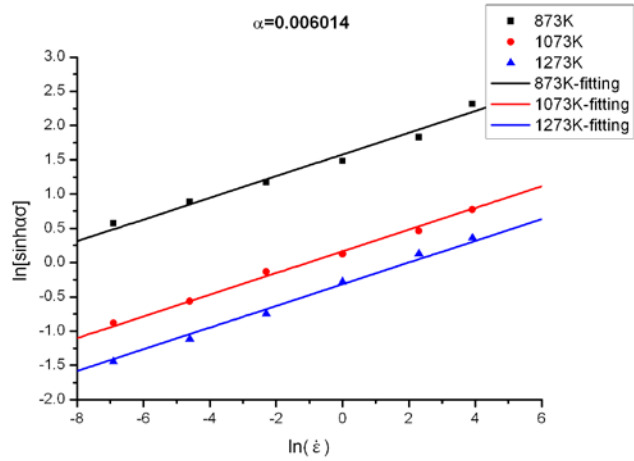
Figure 2.12 Relationships between $\ln[\sinh(\alpha\sigma)]$ and $\ln\dot{\varepsilon}$ at various temperatures and a
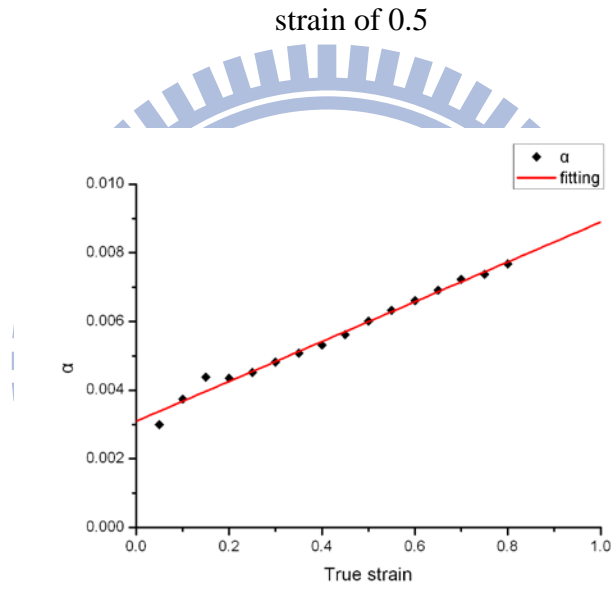
strain of 0.5

Figure 2.13 The value of parameter α in Arrhenius-type constitutive model
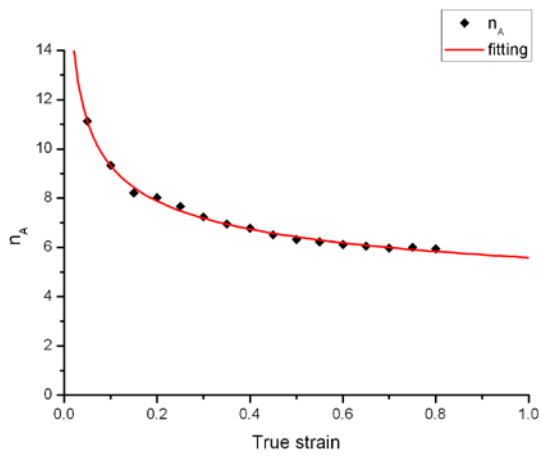
Figure 2.14 The value of parameter n_A in Arrhenius-type constitutive model
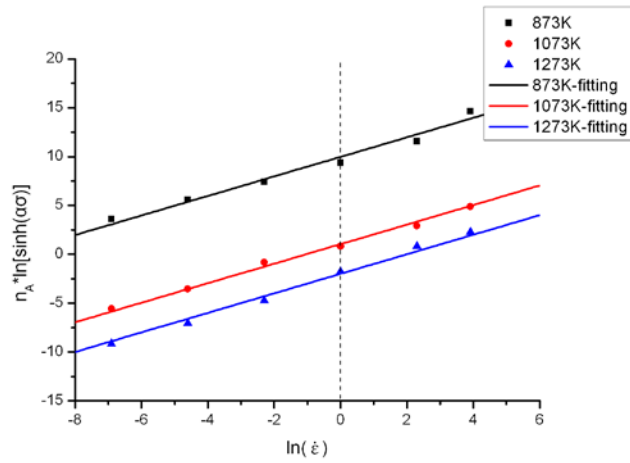
Figure 2.15 Relationships between $n_A \ln[\sinh(\alpha\sigma)]$ and $\ln\dot{\varepsilon}$ at various temperatures and
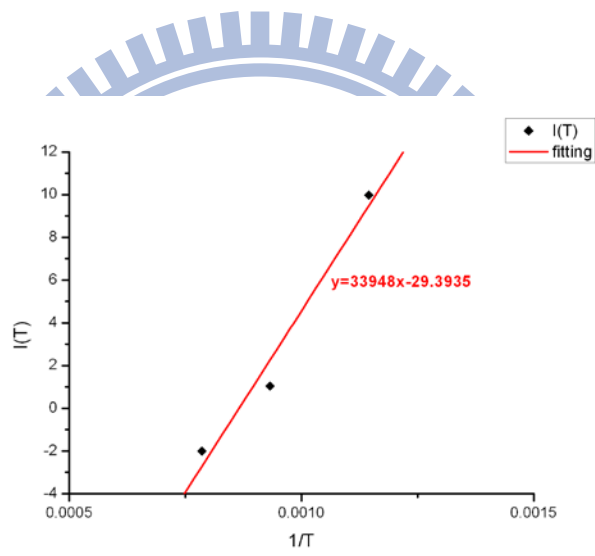
a strain of 0.5

Figure 2.16 Relationships between $I(T)$ and $1/T$ at a strain of 0.5
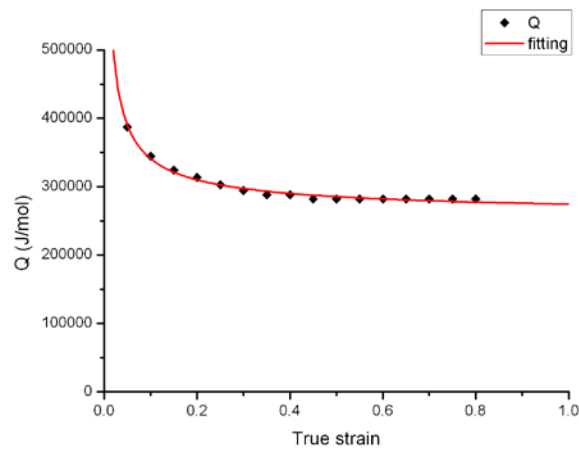
Figure 2.17 The value of parameter Q in Arrhenius-type constitutive model
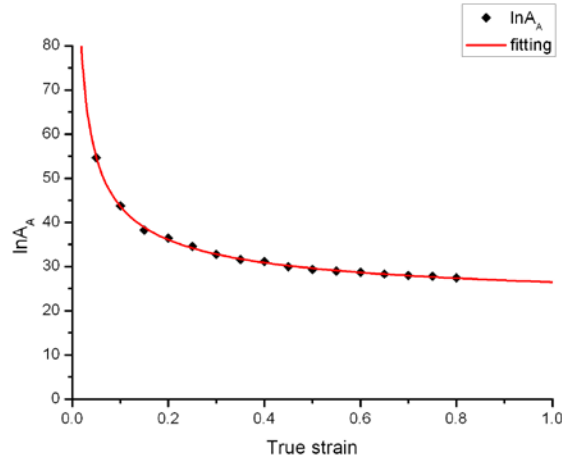
Figure 2.18 The value of parameter $\ln A_A$ in Arrhenius-type constitutive model

Rearranging equation (2.11) yields:

$$n_A \ln[\sinh(\alpha\sigma)] = \ln\dot{\varepsilon} + \frac{Q}{RT} - \ln A_A \tag{2.12}$$

At a particular strain, the y-intercepts of the $n_A \ln[\sinh(\alpha\sigma)]$ vs. $\ln\dot{\varepsilon}$ plot (Figure 2.15) can be expressed as:

$$I(T) = \frac{Q}{RT} - \ln A_A \tag{2.13}$$

From equation (2.13), the value of Q and $\ln A$ can be calculated from the slope and y-intercept of the $I(T)$ vs. $1/T$ plot (Figure 2.16), respectively. Similar procedures were repeated to obtain the value of Q and $\ln A_A$ at various strains (as shown in Figure 2.17 and Figure 2.18).

It can been observed that α, n_A, Q, and $\ln A_A$ significantly vary with strain; therefore, compensation of strain should be taken into account to derive constitutive equation[21]. Rao and Hawbolt [27] introduced that the relationship between strain and the parameters (n_A, Q, and $\ln A_A$) could be expressed as a power equation:

$$Y_i = {D_i}/{\varepsilon^{E_i}} + F_i \tag{2.14}$$

where Y_i is the parameter and D_i, E_i, F_i are constants.

The constant of the power equation for n_A, Q, and $\ln A_A$ are listed in Table 2.3, and α can be expressed as a linear equation with strain as:

$$\alpha = 0.005802\varepsilon + 0.003094 \tag{2.15}$$

Table 2.3 Constant of the power equation for n_A, Q, and $\ln A_A$ in Arrhenius-type constitutive model AISI 1020 steel

	n_A	Q	$\ln A_A$
D_i	3.301756	19415.72	6.767329
E_i	0.328327	0.645673	0.547911
F_i	2.283383	255070.8	19.74261

After the material constants are obtained, the flow stress at a particular strain can be predicted using the equation (2.16) which is rearranged from equation (2.9) and combined the Zener-Hollomon parameter:

$$\sigma = \frac{1}{\alpha}\ln\left\{\left(\frac{Z}{A_A}\right)^{1/n} + \left[\left(\frac{Z}{A_A}\right)^{2/n} + 1\right]^{1/2}\right\} \tag{2.16}$$

The comparison between experimental and predicted flow stress curves under various strain rates (0.001, 0.01, 0.1, 1, 10, and 50 s^{-1}) and temperatures (873, 1073, and 1273 K) is shown in Figure 2.19.

Figure 2.20 shows the correlation between experimental and predicted flow stress using Arrhenius-type constitutive model under range of strain (0.05-0.8 in steps of 0.05), strain rates (0.001-50 s^{-1}), and temperatures (873-1273 K). The correlation coefficient (r) was 0.9875. The correlation between experimental and predicted flow stress using Arrhenius-type constitutive model was higher than that using JC constitutive model.
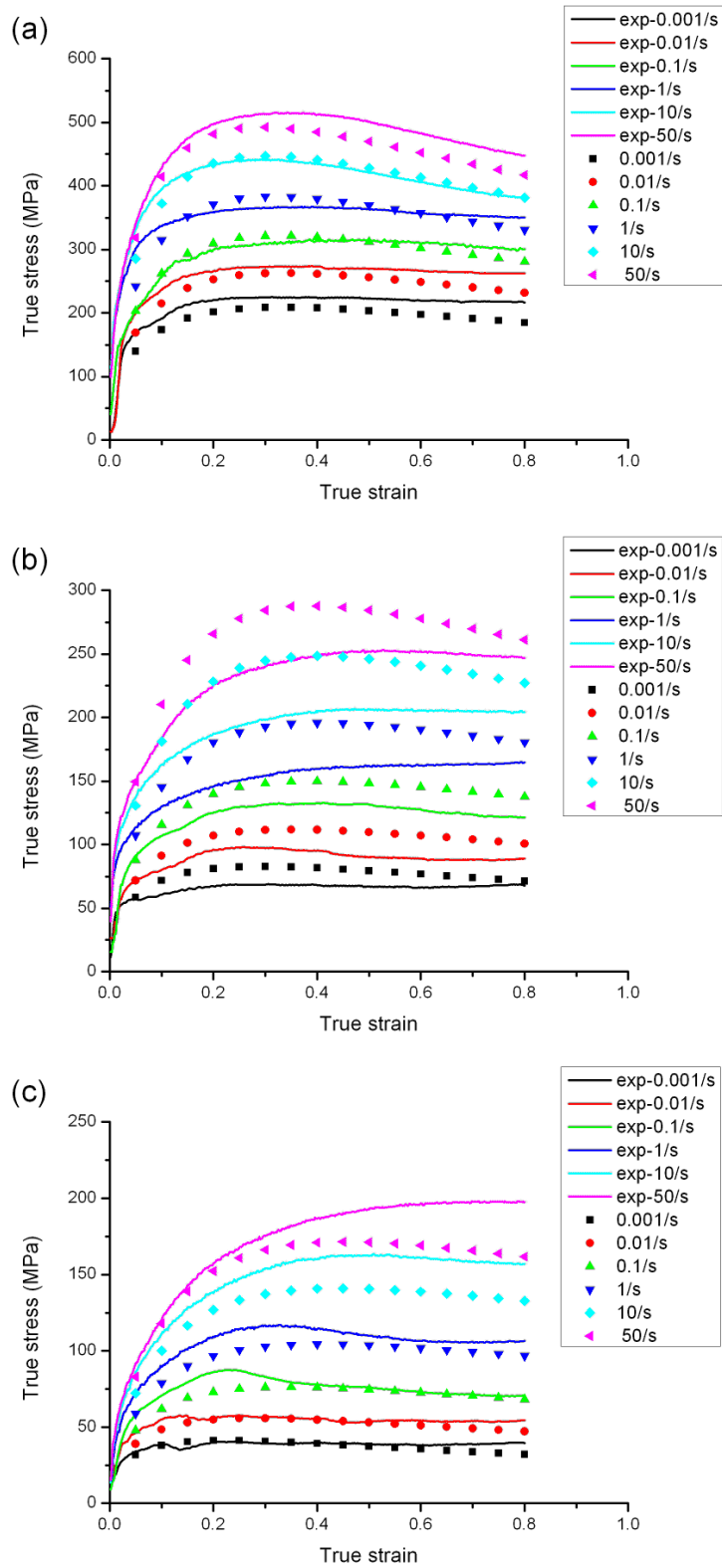
Figure 2.19 Comparison between experimental and predicted flow stress curves using

Arrhenius-type constitutive model under various strain rates at temperatures of (a) 873K, (b)

1073K, and (c) 1273K
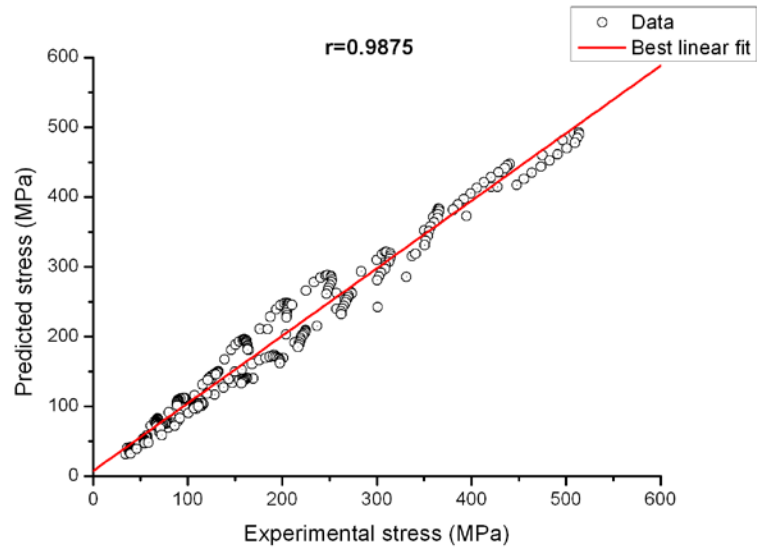
Figure 2.20 Correlation between experimental and predicted flow stress using

Arrhenius-type constitutive model under range of strain (0.05-0.8 in steps of 0.05), strain

rates (0.001-50 s^{-1}), and temperatures (873-1273 K).
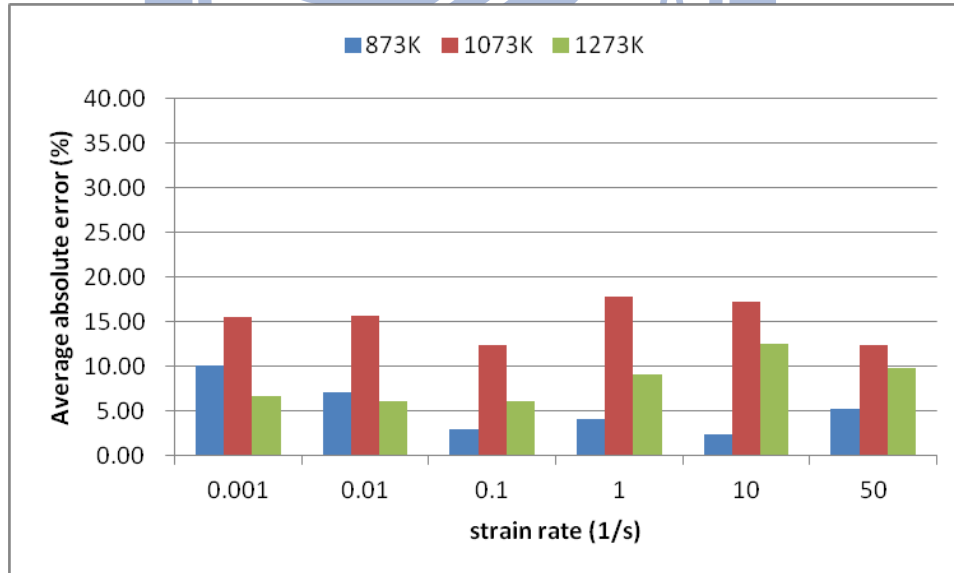
Figure 2.21 Average absolute errors between experimental and predicted flow stress using

Arrhenius-type constitutive model under various strain rates (0.001-50 s^{-1}) and temperatures

(873-1273 K).

Figure 2.21 and Table 2.4 show the average absolute errors between experimental and predicted flow stress using Arrhenius-type constitutive model under various strain rates (0.001-50 s^{-1}) and temperatures (873-1273 K). The average absolute errors between experimental and predicted flow stress for all condition was 9.65%. Although, the errors of prediction at a temperature of 1073K were still large, the accuracy of the prediction using Arrhenius-type constitutive model was acceptable.

Table 2.4 Average absolute errors between experimental and predicted flow stress using Arrhenius-type constitutive model under strain rates (0.001-50 s^{-1}) and temperatures (873-1273 K) (unit: %)

		Strain rate					
		0.001/s	0.01/s	0.1/s	1/s	10/s	50/s
	873K	10.14	7.08	2.99	4.14	2.39	5.29
Temperature	1073K	15.59	15.65	12.46	17.86	17.31	12.37
	1273K	6.73	6.13	6.18	9.16	12.54	9.77

2.3 Summary

The isothermal hot compression tests over a wide range of strains (0.05-0.8), temperatures (873-1273 K), and strain rates (0.001-50 s^{-1}) were performed to obtain the material properties. Two phenomenological constitutive models, Johnson-Cook model and Arrhenius-type model, were then used to predict the flow stress. The comparisons between experimental and predicted flow stresses show that the accuracy of the prediction using Arrhenius-type constitutive model was acceptable. The original flow stress data and predicted flow stress data can be inputted into to the finite element simulations in the chapter 4.

CHAPTER 3 EXPERIMENTS OF TUBE NECK-SPINNING PROCESS

The procedures for conducting the experiments of tube neck-spinning process at elevated temperature were described in this chapter. During spinning process, the temperature distribution on the tube was measured by using infrared camera. Finally, the thickness distribution and outer contour of spun tube were obtained.

3.1 Experimental Procedures

Figure 3.1 illustrates the setup of the spinning machine, where the tube is clamped on the spindle and the axis of two rollers is parallel to the axis of spindle. The movement of two rollers is symmetrically controlled by computer numerical control (CNC) programs. Figure 3.2 shows the dimensions of the roller.
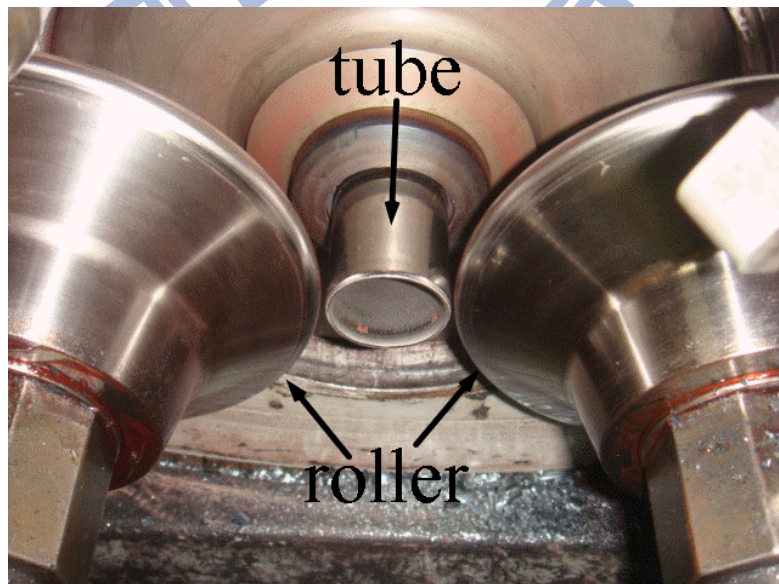
Figure 3.1 Photograph of spinning machine
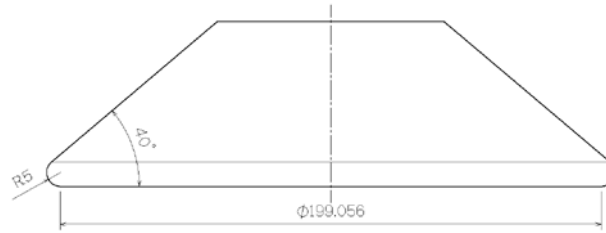
Figure 3.2 Dimension of the roller
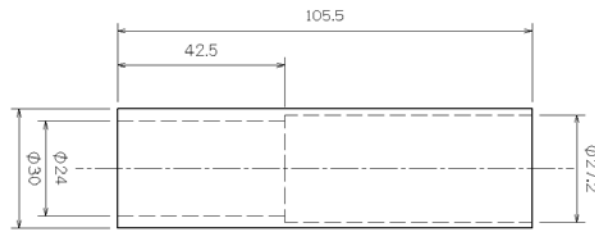
Figure 3.3 Dimension of the tube

The tubes for neck-spinning are manufactured from rod steel using turning and boring. Figure 3.3 shows the dimension of the tube. The tube is divided into two parts with different wall thickness due to the limitation of boring depth. The wall thickness is 1.4 mm at upper region of the tube and 3 mm at remaining part (42.5 mm from the bottom) of the tube. During the experiment, the bottom part of the tube (63 mm from the bottom) is fixed by a clamp, so the influence of the thicker part of the tube will be insignificant.

The procedure for neck-spinning at elevated temperatures was divided into a three-stage sequential process including heating, spinning, and cooling. First, the tube was heated to a specified forming temperature by a high frequency induction heater. The tube was then formed by rollers without heating in the second stage. The tube was clamped on the spindle and rotated at 1800 rpm, and the rollers feeding speed was 1600 mm/min. Six spinning steps were performed sequentially and the roller paths are shown in Figure 3.4. The first to fifth steps were all straight and directed from the top of the tube to the bottom. The sixth step moved

from the end point of fifth step to the bottom of the domed shape along a curve and then moves reversely to the top of the tube. After spinning stage, the tube was cooled to room temperature using compressed air.
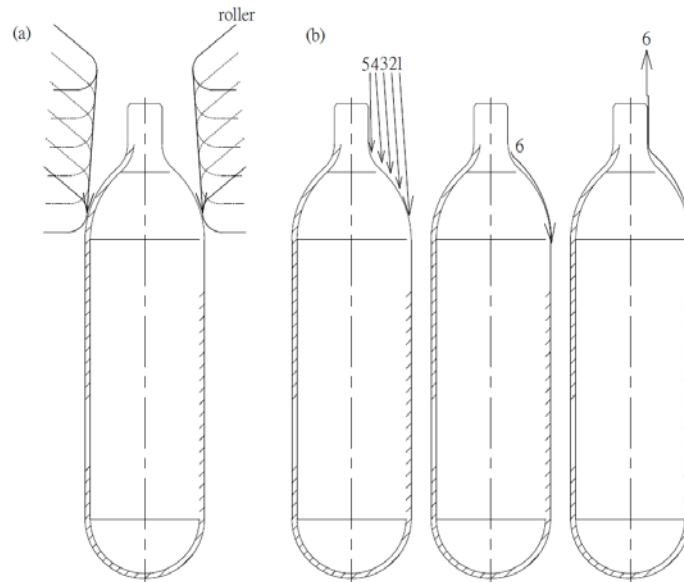
Figure 3.4 Schema of roller moving path (a) first step (b) six steps

3.2 Temperature Measurement

In the experiment, the tube was heated using a high frequency induction heater, which was controlled by a single-point infrared thermometer, until the temperature of monitoring point reached a setting temperature of 950℃. Thus it could be expected that the temperature distribution of the tube was not uniform after heating. Furthermore, there was no heating system to control the temperature of the tube during the spinning stage so the temperature may change as a result of plastic work and heat transfer between the tube, rollers, and environment. Nonuniformity of temperature distribution and the change of temperature with respect to time will result in different material properties. Therefore, in order to construct an accurate finite element analysis, the temperature distribution of the tube should be measured during the spinning stage.

Figure 3.5 Infrared camera (FLIR ThermaCAM-S65)
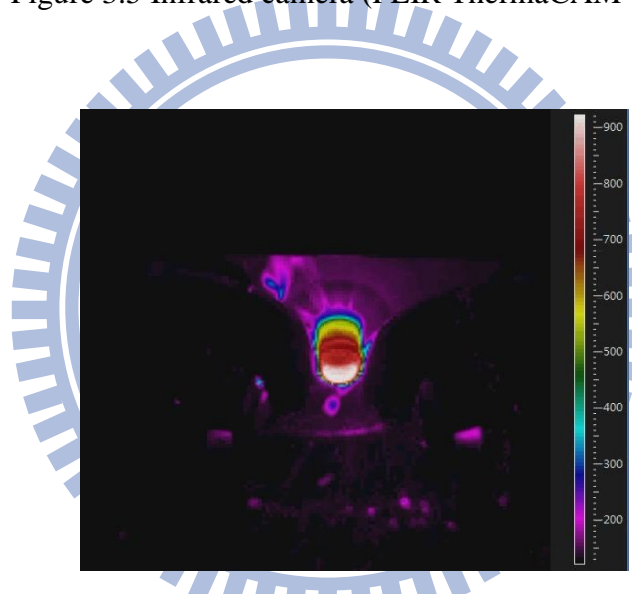
Figure 3.6 Infrared image of the tube during spinning process
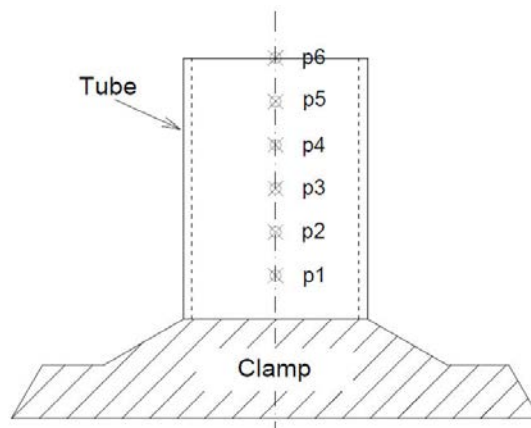
Figure 3.7 Schema of temperature measurement points

Table 3.1 Positions of temperature measurement points

Temperature measurement point	Distance from tube bottom (mm)
p1	70.083
p2	77.167
p3	84.25
p4	91.333
p5	98.417
p6	105.5

During the spinning, the temperature distribution was captured using an infrared camera, FLIR ThermaCAM-S65, as Figure 3.5 shows. The resolution and accuracy of this infrared camera are 320 x 240 pixels and ±2%, respectively. Three ranges of temperature measurement can be chosen in the camera: range Ⅰ, -40~120℃; range Ⅱ, 0~500℃; range Ⅲ, 300~1500℃. The tube was heated to 950℃ so range Ⅲ was chosen for measuring the temperature of the tube. Figure 3.6 shows the captured infrared image. The temperature histories on six measured points were acquired. The measured points were distributed from the clamp to the top of tube with equal distance as shown in Figure 3.7, and the positions of points were listed in Table 3.1.

Figure 3.8 shows the measured temperature histories during the spinning process. On the whole, the temperature decreased as time went on because of heat transfer; however, the local temperature rapidly increased in the periods of spinning steps except first step. During first step, the measured temperature was not probably real because the surface of the tube was covered with oxides. Figure 3.9 shows that sparks occurred at first spinning step, which implied that the oxides were removed. During the other steps, the local increasing temperature should be a result of plastic work because the sequence of increasing temperature followed the roller forming path. For example, in second step, the temperature at p6 increased first and

then the temperature at p5 and p4 increased sequentially while the rollers moved from top of the tube to the bottom.
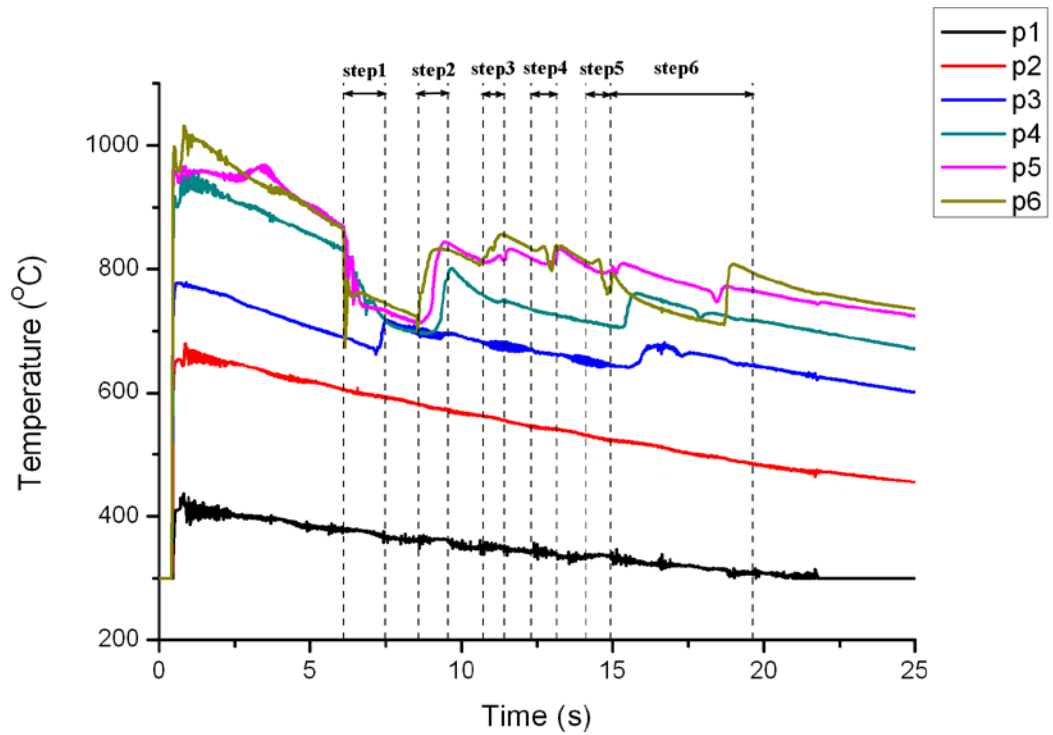
Figure 3.8 Measured temperature histories of the tube
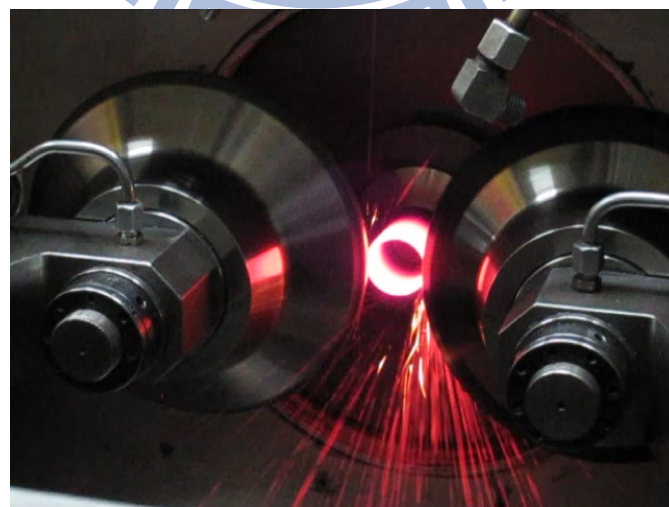
Figure 3.9 Sparks at first spinning step

3.3 Experimental Results

Figure 3.10 shows the results of neck-spinning process at elevated temperatures on the tubes after each of the six steps. A bell-mouth occurred at the top of the tube in the first five steps. Furthermore, small bulges, which were formed from the build-up of material at the end of roller forming path, were clearly displayed in these spun tubes.

Figure 3.10 Six steps of spun tubes
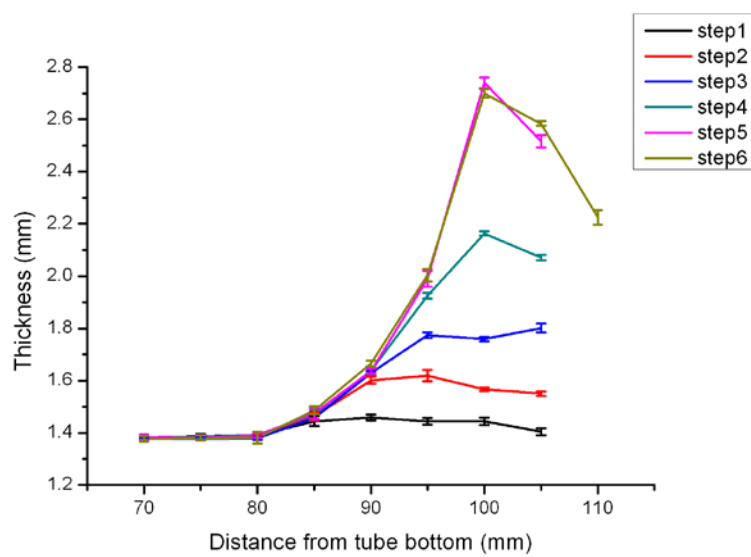
Figure 3.11 Thickness of experimental spun tubes
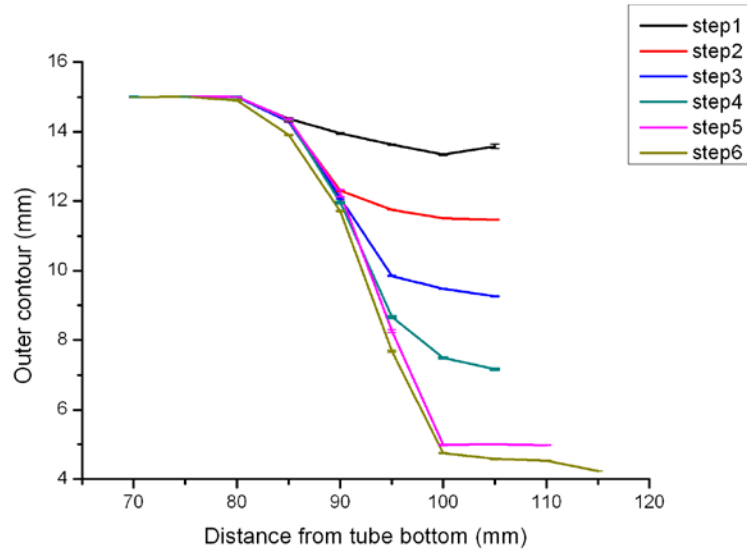
Figure 3.12 Outer contour of experimental spun tube

Figure 3.11 and Figure 3.12 show the thickness distribution and outer contour of experimental spun tubes, respectively. The first five steps involved rough forming and most of the deformation was completed during these steps. The final step was used to diminish the small bulges and form the design shape precisely. Therefore, from the first to the fifth step, the thickness near the top of the tube increased significantly as spinning step increased, and the change of thickness during the sixth step was minimum. Similarly, the outer contour near the top of the tube decreased significantly as spinning step increased from the first to the fifth step.

3.4 Summary

The experiments of neck-spinning process of tubes at elevated temperatures were performed. The temperature distribution on the tube was measured during the spinning process, and the measured temperatures indicated that the temperature change of the tube was significant during the process and the local increasing temperature was a result of plastic work in the period of forming steps. The data of measured temperatures can be inputted into the

finite element simulations as the thermal boundary condition in chapter 4. The experimental results on thickness distribution and outer contour of the tube can be used to validate the simulated results in chapter 4.

CHAPTER 4 FINITE ELEMENT ANALYSIS AND VERIFICATION

Via material tests, material properties of AISI 1020 steel for the finite element analysis on neck-spinning process at elevated temperatures were obtained; moreover, experiments of neck-spinning process at elevated temperatures were performed. In this chapter, the three-dimensional finite element model was firstly constructed to simulate the neck-spinning process. The comparisons between experimental and simulation results on thickness distribution and the outer contour of the spun tube were then discussed to verify the finite element model.

4.1 FEA program – Abaqus/Explicit

Abaqus/Explicit (Dassault Systemes) is commercial finite element analysis software which is suited to simulate the quasi-static and transient dynamic problem. The ability of Abaqus/Explicit to handle severely nonlinear behavior such as contact makes it very effective for the simulation of many quasi-static problems [34].

Because the contact region between the tube and the roller changes rapidly and the deformation is large during the neck-spinning process, the nonlinearity of the problem is severe. Therefore, Abaqus/Explicit is an ideal choice for this study.

4.2 Finite Element Model and Boundary Conditions

This study used the commercial software Abaqus/Explicit to simulate the neck-spinning of a tube at elevated temperatures. The following assumptions were adopted to establish the FEA model:

1. The tube was isotropic and homogenous with an elastic-plastic response,

40

2.   The rollers were treated as rigid bodies,

3.   The relative tangential speed between the rollers and tube was zero during contact.

Figure 4.1 shows the FEA model. Only a partial tube (42.5 mm in length) was constructed in the model because the bottom part of the tube (63 mm from the bottom) was fixed by a clamp during the experiment. All degrees of freedom were fixed at the bottom nodes of the model in the simulation. Eight-node solid elements with full integration were chosen for the simulation. Figure 4.2 shows the mesh model of the tube. Three layers of elements were constructed along the thickness direction and 60 elements were constructed along the circumferential direction. Along the axis direction, 28 elements were in the large deformation zone (27.5 mm in length) and 10 elements were in the remaining zone. A total of 9,360 nodes and 6,840 elements were constructed in the FEA model.
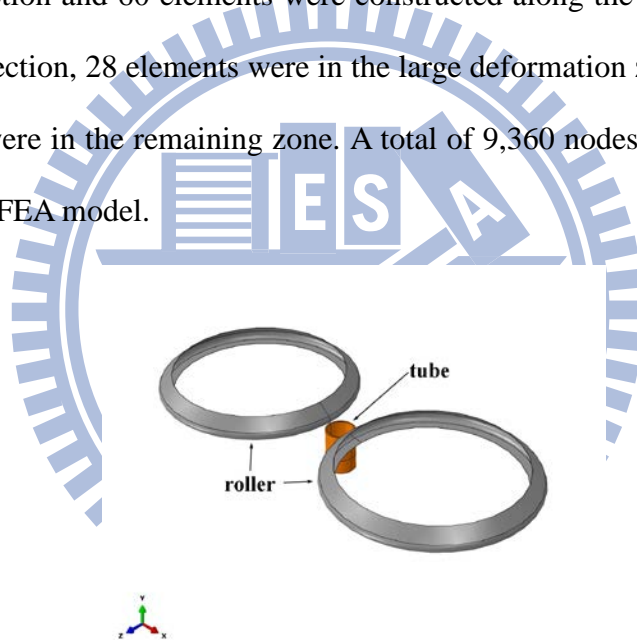
Figure 4.1 Finite element model
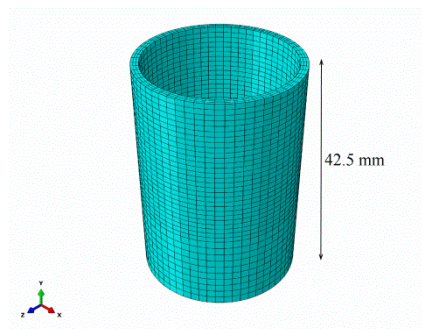
Figure 4.2 Mesh model of the tube

For the boundary conditions of rollers in the simulation, the movements of roller were according to the experimental roller forming paths, as shown in Figure 3.4. The paths of the first to fifth steps directed from the top of the tube to the bottom. However, because the contact problem occurred in FE analysis while the roller touched the top surface of the tube; therefore, in the FE analysis, the roller path was modified into two segments, as shown in Figure 4.3. Firstly, the roller moved along the radial direction to the intersection point of original path and modified path to make sure that the roller surface perpendicularly contacted to the tube surface. Then the roller followed the remaining original path.

original path

modified path
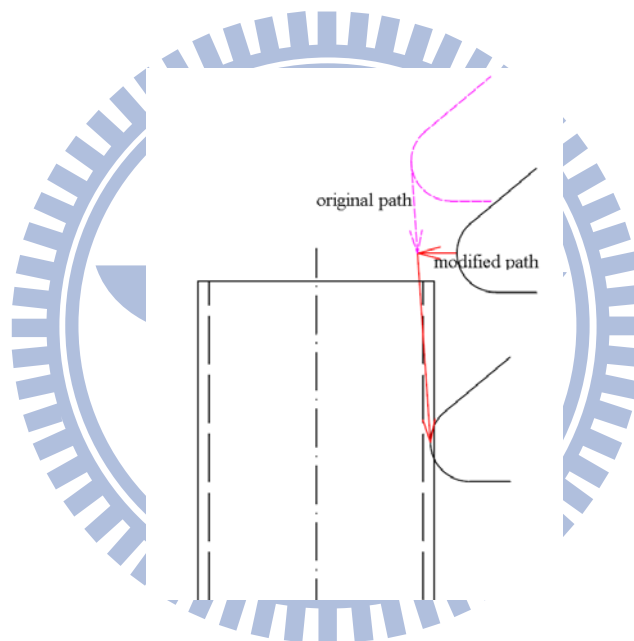
Figure 4.3 Modification of roller forming path in the simulation
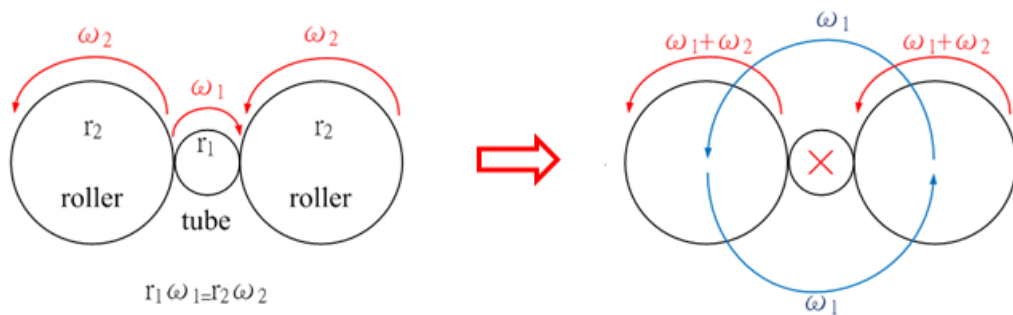
Figure 4.4 Schema of the movement of rollers
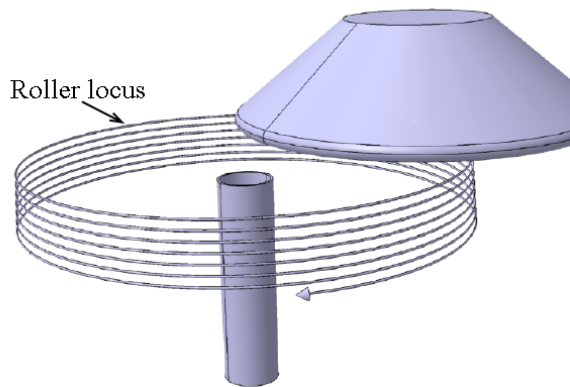
Figure 4.5 Schema of roller locus in the simulation
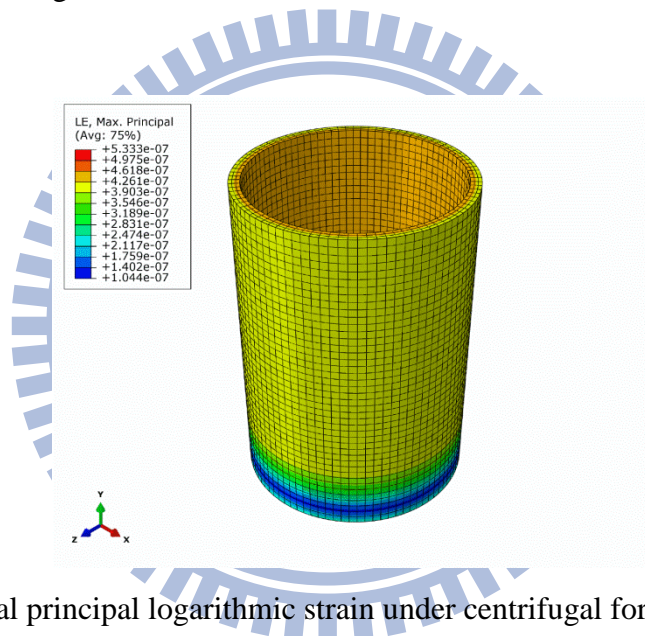
Figure 4.6 Maximal principal logarithmic strain under centrifugal force at a rotational speed

of 1800 rpm and a temperature of 950 ℃

In the real forming process, the tube rotates around its axis and the rollers rotate freely while making contact with tubes. However, numerous rotations of a deformable body may result in a volume change and numerical error in FE analysis [13] [35]. Therefore, in this study, the tube was fixed and the rigid rollers revolved around the axis of the tube. Figure 4.4 shows the schema of the movement of rollers. The revolving speed was equal to the rotational speed of the spindle in the experiment. The roller locus in the simulation was shown in Figure 4.5.

The tube was fixed in the simulation so the centrifugal force acting on the tube in the real process was neglected in the simulation. Figure 4.6 shows the strain distribution of the tube under centrifugal force at a rotational speed of 1800 rpm and a temperature of 950 ℃. The maximal strain value was minute; therefore, the neglect of centrifugal force acting on the tube was acceptable in the simulation. Furthermore, the rollers did not rotate freely in the simulation; in contrast, the rotational speed of the roller on its own axis was given for the entire simulation time. According to the assumption of zero relative tangential speed between the rollers and tube, the rotational speed of the roller on its own axis could be calculated from the rotational speed of the spindle in the experiment as equation (4.1).

$$\omega_{roller} = \omega_{spindle} \times r_{tube}/r_{roller} \tag{4.1}$$

where ω_{roller} is rotational speed of the roller, $\omega_{spindle}$ is the rotational speed of the spindle in the experiment, r_{tube} is the instant distance from the tip of the roller to the axis of the tube, and r_{roller} is the radius of roller.

For the contact condition, the interfacial friction between the tube and rollers was described by Coulomb's friction model which is most commonly expressed as:

$$f_s = \mu p \tag{4.2}$$

where f_s is the friction shear stress, μ is the coefficient of friction, and p is the compressive normal stress to the interface. In a hot working process, the typical coefficient of friction was determined experimentally to be 0.4 [36]. Thus, in this study, the coefficient of friction in the interface between the tube and rollers was assumed to be 0.4.

For the thermal boundary conditions, the temperature change was simplified to be linear with respect to time and the temperature at the same height of the tube was assumed to be equal in the simulation. According to the measured temperatures, as shown in Figure 3.8, a linear line was used to fit the temperatures histories of the tube at each measured point. For example, the fitted temperature histories of step 1 and step 2 were as shown in Figure 4.7 and Figure 4.8, respectively.
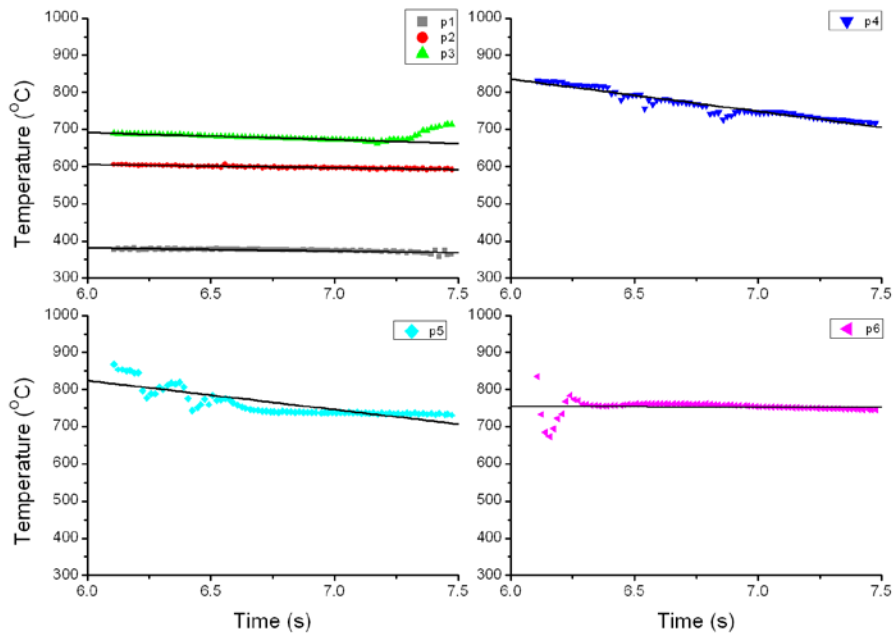
Figure 4.7 Fitted temperature histories of step 1
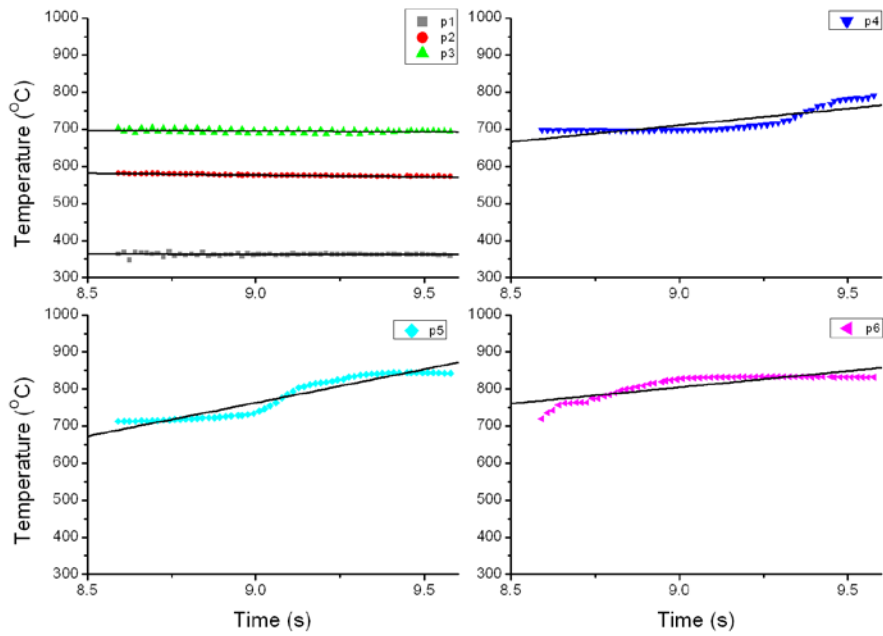
Figure 4.8 Fitted temperature histories of step 2

Table 4.1 Coefficient of thermal expansion

Temperature ($^\circ$C)	Coefficient of thermal expansion
-100	1.08×10^{-05}
0	1.17×10^{-05}
20	1.19×10^{-05}
100	1.25×10^{-05}
200	1.30×10^{-05}
300	1.36×10^{-05}
400	1.41×10^{-05}
500	1.45×10^{-05}
600	1.49×10^{-05}
1500	1.49×10^{-05}

At high temperatures, the material properties are sensitive to strain rates. In this case, the strain rate value was as high as $30s^{-1}$ during the hot neck-spinning process. Therefore, the finite element simulation should include the strain rate effect of flow stress. Because the predicted flow stresses using Arrhenius-type constitutive model were still not accurate enough, the original flow stress data obtained from compression tests were firstly inputted into the simulation. The effect of the simulation using predicted flow stresses will be considered later. The coefficient of thermal expansion adopted in the simulation was derived from the material database of commercial software DEFORM. Table 4.1 lists the coefficient of thermal expansion at various temperatures.

To reduce the computational time, the mass scaling factor was firstly chosen as 50, and the process was accelerated twice during the simulation. The number of increments was relatively large during the simulation; therefore, a double-precision option was used to avoid the effect of round-off errors.

4.3 Assessment of Mass Scaling Factor

For the explicit analysis, increasing mass scaling factor is a practice to reduce the computational time. This is especially important for time-consuming element type, e.g. solid element with full integration. Larger mass scaling factor means that the initial time increment is larger. However, too large increment will result in contact instability and consequent numerical error.

Several mass scaling factor were first tested in the simulation of neck-spinning process at elevated temperature. Furthermore, in order to prevent the mesh distortion, only first four steps of spinning were carried out in these simulations. Table 4.2 lists the computational time of various mass scaling factors. The computational time increased as the factor decreased.

To make sure that the inertia effects due to mass scaling do not significantly affect the simulation results, the kinetic energy of the deforming material should not exceed a small fraction (typically 5% to 10%) of the internal energy throughout most of the simulation [37]. Figure 4.9 shows the ratio of the kinetic energy to the internal energy. The ratio increased slightly as mass scaling factor increased. The ratio was below 1% throughout entire simulation period except the time was less than 0.02 s; consequently, the dynamic effects in these cases were insignificant.

Table 4.2 Computational time of simulation using various mass scaling factors

Mass scaling factor	Computational time
75	6hours 33minutes
50	8hours 02minutes
25	11hours 33minutes
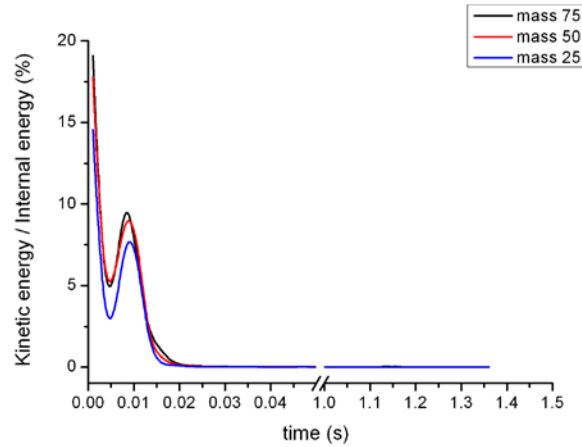
Figure 4.9 Ratio of the kinetic energy to internal energy using various mass scaling factor

Figure 4.10 shows the influences of the mass scaling factor on the thickness distribution. The simulation results using mass scaling factors of 50 and 25 were close to each other, whereas the result using factor of 75 was different from the others. Figure 4.11 shows the influences of the mass scaling factor on roller radial force. As the factor increased, the inertia of the tube increased, therefore the shock of the roller radial force increased. In summary, it was efficient and acceptable to choose the mass scaling factor as 50.
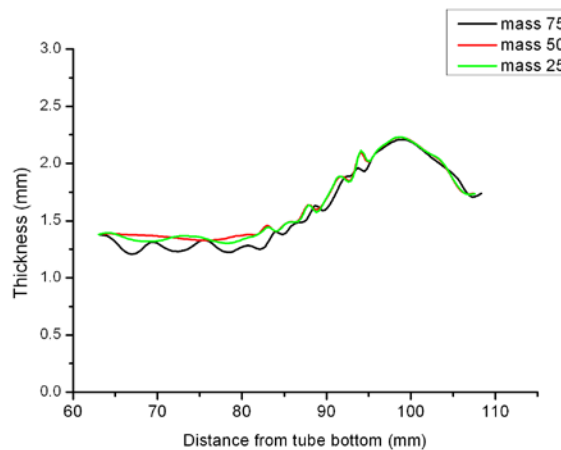
Figure 4.10 The influences of the mass scaling factor on thickness
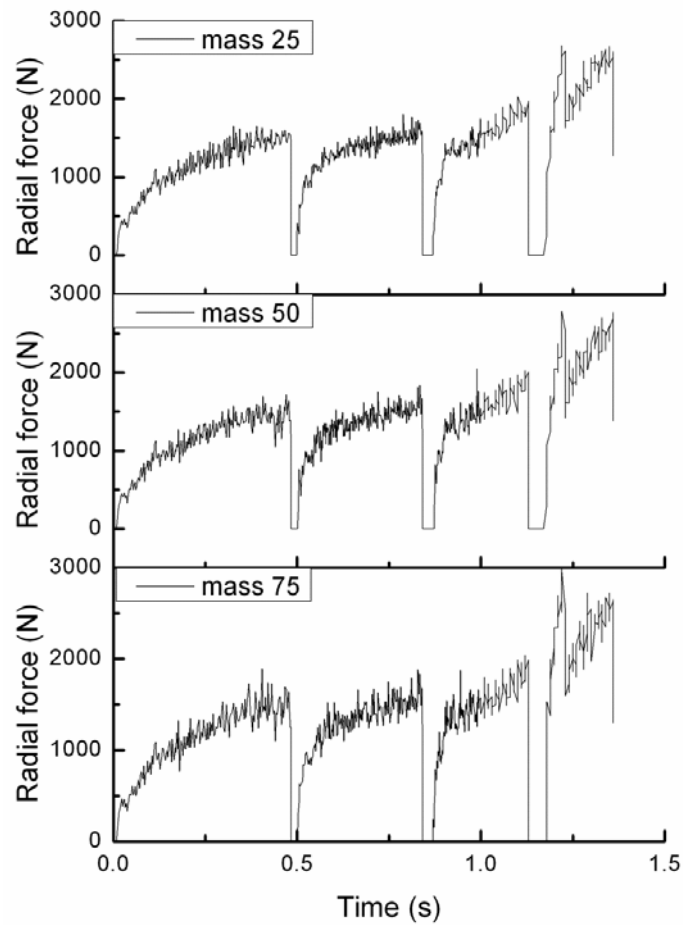
Figure 4.11 The influences of the mass scaling factor on radial force of roller

4.4 Remeshing (rezoning) technique

Figure 4.12 shows the simulation result after the fourth neck-spinning step. The maximal value of the equivalent plastic strain was at the neck of the tube. At this region, the meshes distorted severely and the quality of meshes decreased. Poor mesh quality may result in additional numerical errors; therefore, redefining the mesh system was necessary. Abaqus/Explicit provides a function called "ALE adaptive meshing" to maintain a high-quality mesh throughout an analysis [38], but this function is only available while using the reduced integration element. Hence, ALE adaptive meshing was unsuitable for this study, and remeshing should be manually executed.
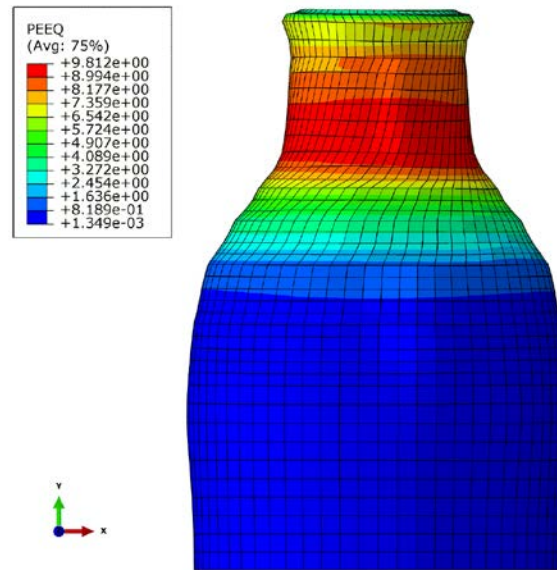
Figure 4.12 Equivalent plastic strain after four steps of spinning

Remeshing consists of two procedures. The first involves assigning a new mesh system to the tube, and the second entails transferring information from the old to the new mesh using interpolation [39]. Therefore, the coordinates of old nodal points on the inner and outer surface of the tube were output to obtain the average contour of the tube after the fourth simulation step; in addition, the new geometric model of the tube was axis-symmetrically constructed according to the average contour. Figure 4.13 shows the mesh model of the tube before and after remeshing. Although there was a difference between these two mesh models because the new model was treated as axis-symmetric, the new contour of the tube was closed to the old one and the distorted meshes were diminished successfully.
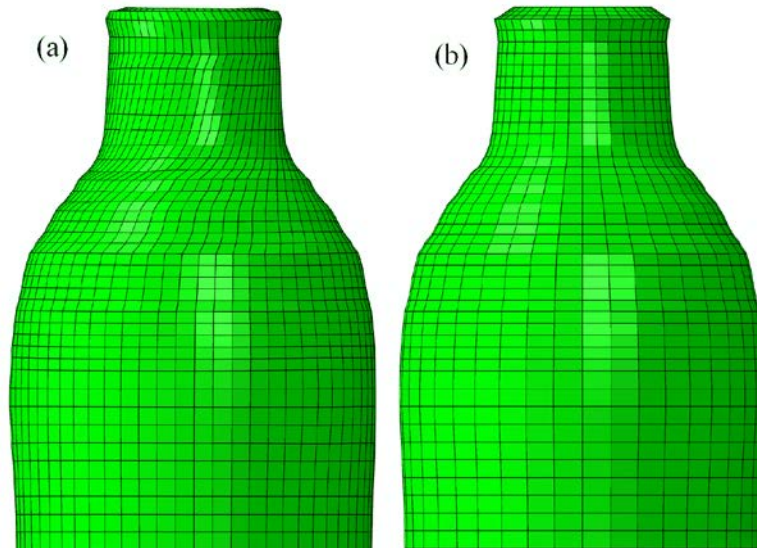
Figure 4.13 Mesh model of the tube after four steps of spinning (a) before remeshing (b)
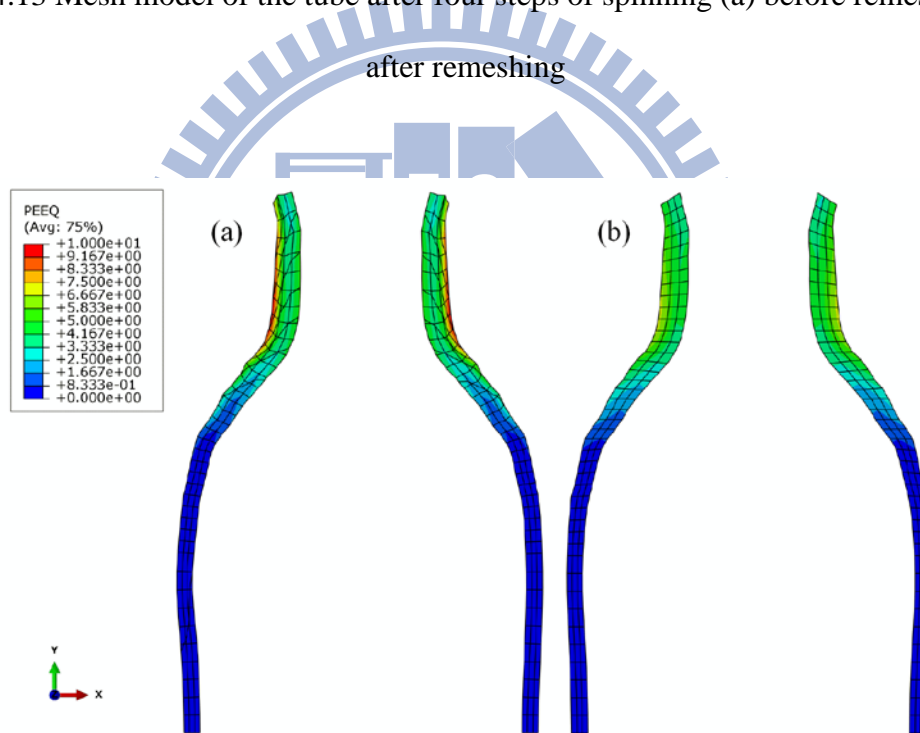
after remeshing

Figure 4.14 The distribution of equivalent plastic strain after four steps of spinning (a)

before remeshing (b) after remeshing

For the second procedure of remeshing in this study, only the simulation results of equivalent plastic strain of the old model were transferred to the new model; therefore, the elastic deformation of the tube occurring in previous steps were neglected. The data of equivalent plastic strain were output at old nodal points and then mapped to new nodal points

using interpolation. In Abaqus/Explicit, the initial condition of hardening can be input into a simulation, but the strain value must be uniform in one element. Therefore, the equivalent plastic strain of each new element was averaged from the values on its eight corresponding nodal points. Figure 4.14 shows the distribution of equivalent plastic strain before and after remeshing. Because the strain value must be uniform in each element, the equivalent plastic strain exhibited little difference between the old and new model near the outer surface; however, the simulation result of equivalent plastic strain of the old model was successfully transferred to the new model at most regions of the tube.

Figure 4.15 shows the simulation result after the fifth neck-spinning step. The meshes distorted severely again and the quality of meshes decreased; therefore, the mesh system needed to redefine again. Figure 4.16 shows the mesh model of the tube before and after remeshing. Figure 4.17 shows the distribution of equivalent plastic strain before and after remeshing.
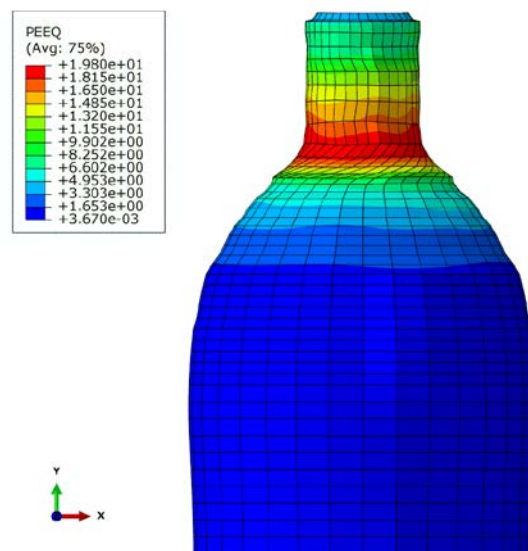
Figure 4.15 Equivalent plastic strain after five steps of spinning
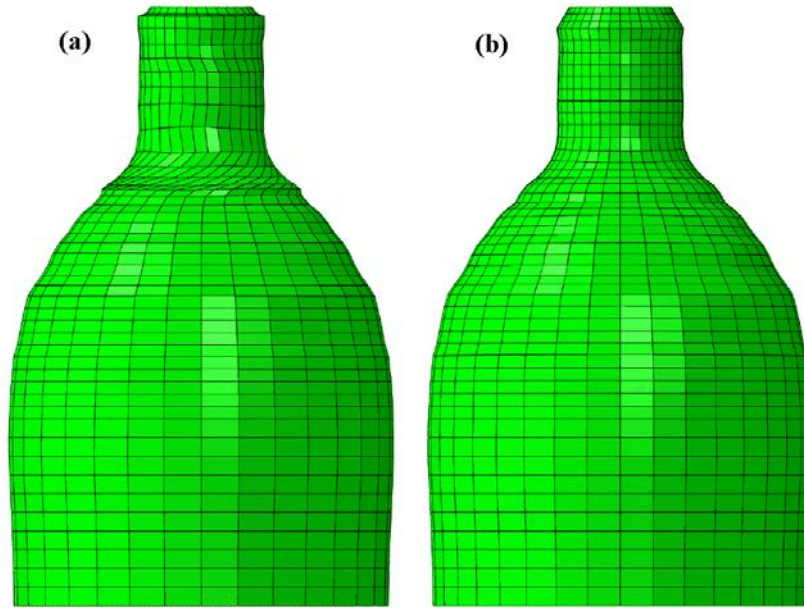
Figure 4.16 Mesh model of the tube after five steps of spinning (a) before remeshing (b)
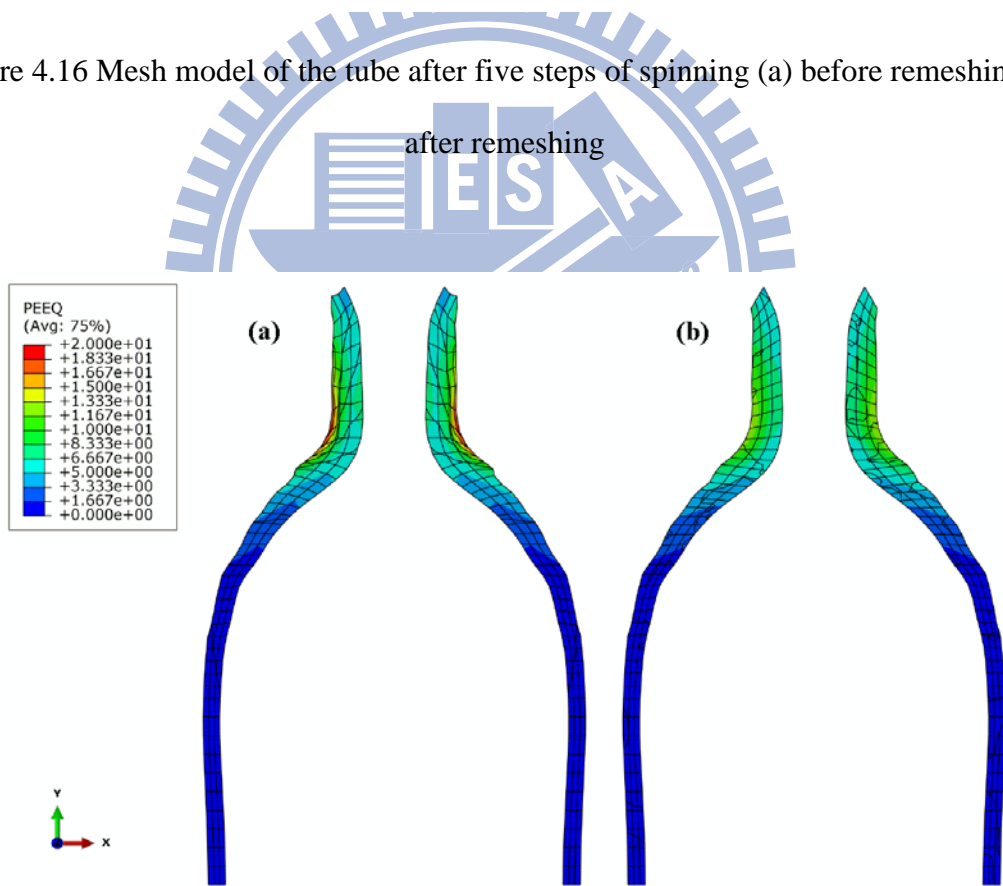
after remeshing

Figure 4.17 The distribution of equivalent plastic strain after five steps of spinning　(a)

before remeshing (b) after remeshing

4.5 Verification on Finite Element Analysis

The total time of the six-step spinning process was 4.1885 seconds in the simulation. To reduce the computational time, the mass scaling factor was chosen as 50 and the process was accelerated twice during the simulation; therefore, the initial time increment was 4.824×10^{-7} second. With the current chosen mass scaling factor and time scaling factor, the simulation was completed in 20 hours and 10 minutes using a personal computer with 2 CPUs (Intel Xeon Nehalem Quad-Core E5530) and 8 GB RAM.

To make sure that the inertia effects due to mass scaling do not significantly affect the simulation results, the kinetic energy of the deforming material should not exceed a small fraction (typically 5% to 10%) of the internal energy throughout most of the simulation [37]. Figure 4.18 shows the ratio of the kinetic energy to the internal energy, which was below 1% throughout entire simulation time except the beginning of the simulation; consequently, the dynamic effects in these cases were insignificant.

Figure 4.19 shows the simulation results of equivalent plastic strain after each spinning stage. The maximum value of the equivalent plastic strain was approximately 20 at the top of the tube. This equivalent plastic strain was quite large, so it would be difficult to produce this tube at room temperature in so few steps. At first five steps, a bell-mouth occurred at the top of the tube and small bulges occurred at the tube surface. These same phenomena display in the experiment (Figure 3.10).
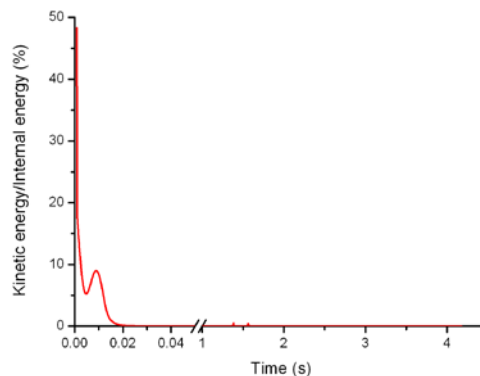
Figure 4.18 Ratio of the kinetic energy to the internal energy
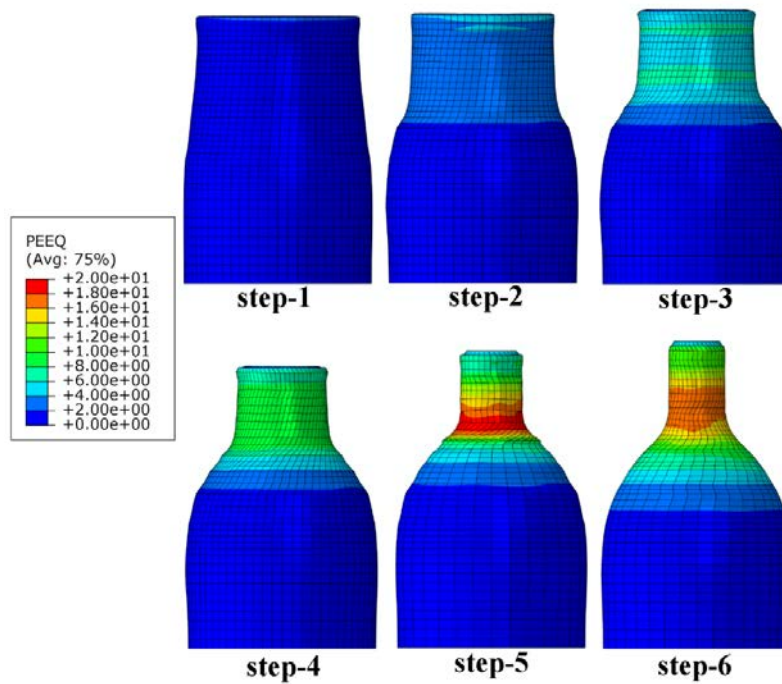
Figure 4.19 Equivalent plastic strain of each step
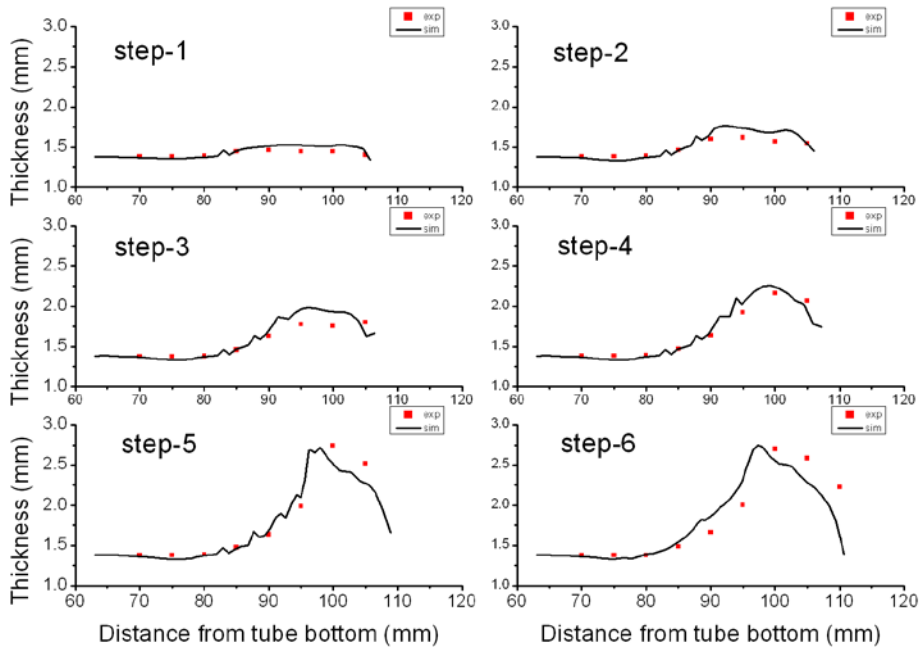
Figure 4.20 Comparison between experimental and simulated results for the thickness

distribution of the spun tube

For the detailed verifications, Figure 4.20 shows the comparison of thickness distribution of the tube between the simulated and experimental results after each step. In both simulation and experiment, the thickness increased as the spinning process increased except the sixth step. The deviations between experimental and simulated results for the thickness of the tube were listed in Table 4.3. Regarding thickness, the average deviations of the first and the sixth step between the simulation and experiment were 2.72%, 3.18%, 4.76%, 3.39%, 4.31%, and 8.94%, respectively. During the first five steps, the simulated thickness distribution corresponded well with those of the experiment. The deviations of thickness between the simulation and the experiment increased slightly during the final step, but the tendency was consistent. Maximal deviation occurred at the top of the tube during the final step.

Table 4.3 Deviations between experimental and simulated results for the thickness of the tube (unit: %)

Position	Step1	Step2	Step3	Step4	Step5	Step6
70	0.77	0.76	0.49	0.95	0.88	0.58
75	2.20	3.52	3.40	3.96	3.65	3.67
80	1.06	1.10	0.63	1.43	1.28	0.48
85	0.76	0.03	0.47	0.38	0.99	3.72
90	4.01	4.53	4.15	3.56	3.43	11.74
95	5.47	7.24	10.70	6.42	6.44	16.07
100	5.17	7.75	9.87	3.62	8.28	5.20
105	2.30	0.52	8.33	6.76	9.58	11.60
110	x	x	x	x	x	27.42
Average	2.72	3.18	4.76	3.39	4.31	8.94

Figure 4.21 shows the comparison of outer contour of the tube between the simulated and experimental results after each step. The deviations between experimental and simulated results for the thickness of the tube were listed in Table 4.4. Regarding the outer contour, the average deviations from the first to the sixth step between the simulation and experiment were 0.92%, 1.17%, 1.12%, 1.27%, 1.24%, and 1.40%, respectively; hence, the simulated outer contour corresponded accurately with the experimental results.
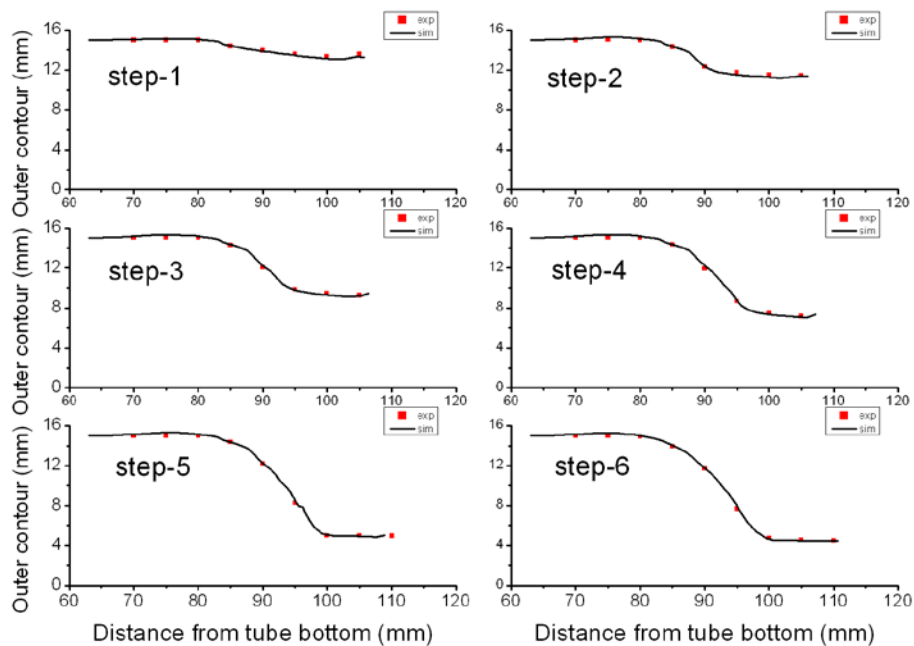
Figure 4.21 Comparison between experimental and simulated results for the outer contour

of the spun tube

Three factors may cause a deviation between the simulation and experiment results. First, the remeshing technique was conducted only after the fourth and the fifth steps; therefore, the quality of the meshes may become poor during the simulation and result in additional numerical errors. Second, the temperature at the same height was assumed to be equal in the simulation; however, in reality, the temperature gradient existed throughout the thickness direction of the

tube. In Figure 3.6, it could be found that the temperature on the inside surface of the tube was higher than that on the outside surface of the tube during the spinning process. Temperature variation affects the material properties and the simulation accuracy. Finally, in the simulation, the roller forming path was modified into two segments, and the first segment was along the radial direction to prevent the contact problem. The roller moved along radial resulted in thinning wall thickness of the tube; therefore, the thickness on the top of the tube was relatively thinner than that on the other position.

Table 4.4 Deviations between experimental and simulated results for outer contour of the tube (unit: %)

Position	Step1	Step2	Step3	Step4	Step5	Step6
70	0.38	0.64	0.69	0.67	0.73	0.70
75	0.96	1.82	2.00	1.99	1.97	1.84
80	0.55	0.95	1.06	1.07	1.02	0.82
85	0.31	0.22	0.49	0.13	0.02	1.09
90	0.46	0.51	1.06	2.25	0.10	0.48
95	1.15	2.17	0.78	0.80	2.78	4.01
100	1.55	2.14	1.85	1.73	2.04	1.09
105	2.01	0.91	1.00	1.50	1.29	1.62
110	x	x	x	x	x	0.92
Average	0.92	1.17	1.12	1.27	1.24	1.40

Although a slight deviation exists between the simulation and experimental results, the FE model for the tube neck-spinning process at elevated temperatures is still reliable. The FE model can be used to determine the proper parameters for the neck-spinning process. This usage is more efficient than experiments that depend on trial and error.

4.6 Influence of coefficient of friction

In the above simulation, the coefficient of friction in the interface between the tube and rollers was assumed to be 0.4. This coefficient is typical for hot working; however, this actual contact property is difficult to measure in tube spinning at elevated temperatures. Therefore, various coefficients of friction (0, 0.1, 0.2, 0.3, 0.4, and 0.5) were tested in the simulations. Furthermore, in order to avoid the mesh distortion problem, only first four steps of spinning were carried out in these simulations.
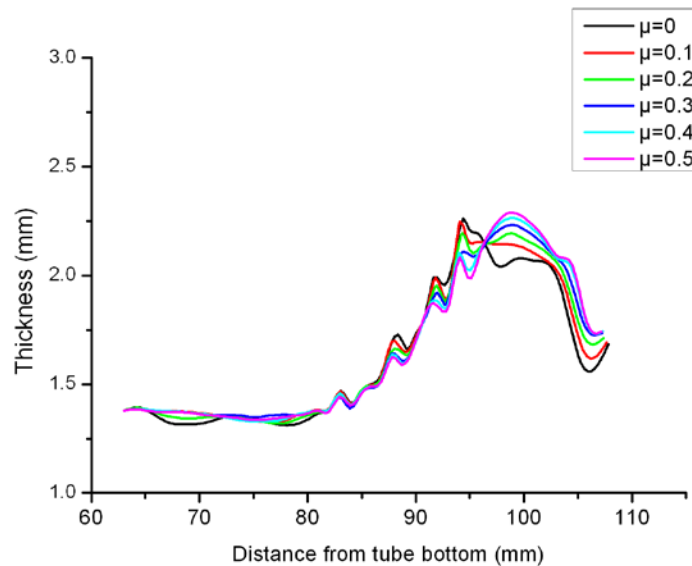
Figure 4.22 The influences of the coefficient of friction on thickness distribution

Figure 4.22 shows the influences of the coefficient of friction on thickness distribution. The tendency of simulated results using various coefficients of friction was consistent. Figure 4.23 shows the influences of the coefficient of friction on outer contour, and the simulated results were close to each other. Figure 4.24 shows the influence of the coefficient of friction on twisting angle of the tube, which is defined as the twisting angle between the top and the bottom of the tube. The twisting angle increased significantly as the coefficient of friction increased. Therefore, measuring the twisting angle in an experiment can verify the coefficient

of friction in a simulation. Possible methods for showing the twisting angle include printing circular grids [15] and sketching longitudinal lines [40] on the tube surface. However, these marks will disappear after tube spinning at elevated temperatures, so it is still difficult to measure the twisting angle of the spun tube.
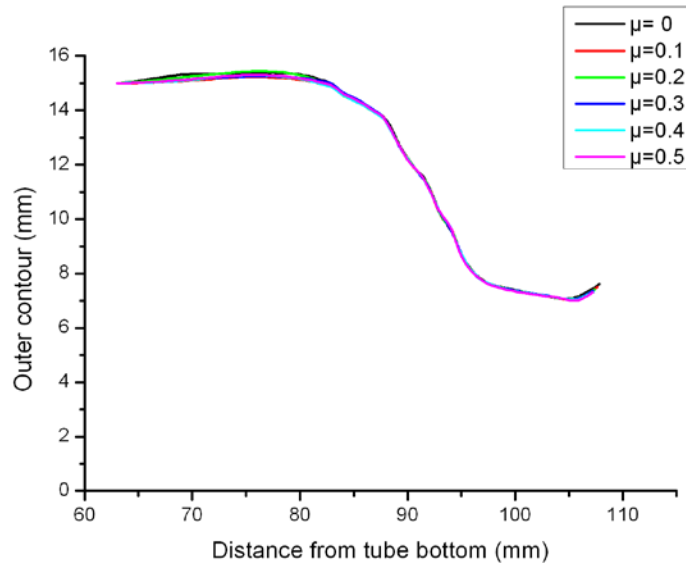
Figure 4.23 The influences of the coefficient of friction on outer contour
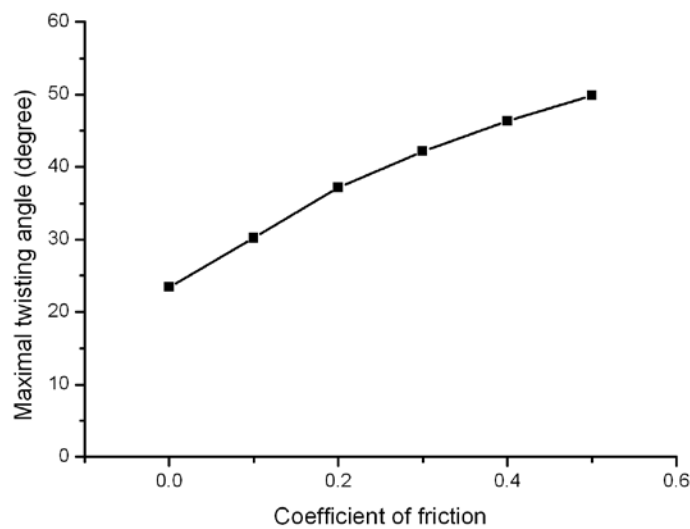
Figure 4.24 The influence of the coefficient of friction on twisting angle
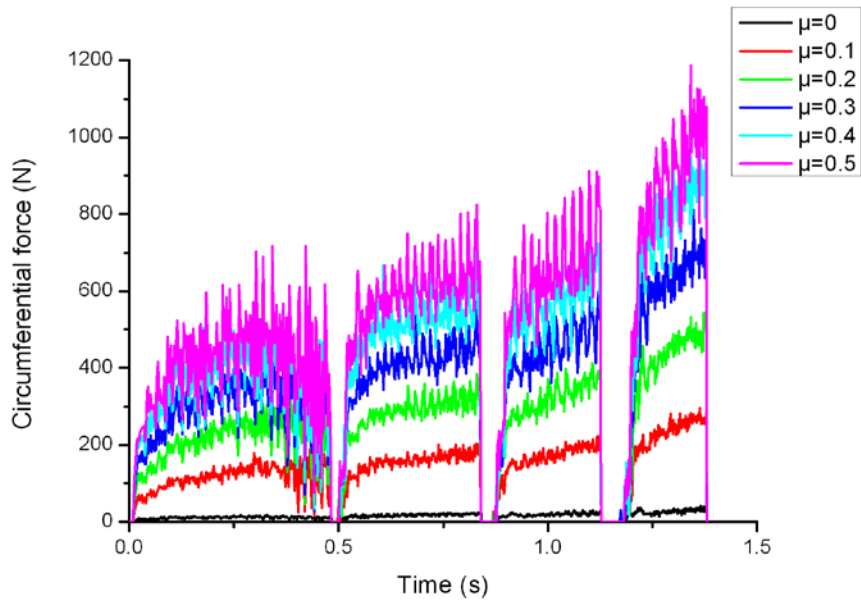
Figure 4.25 The influence of the coefficient of friction on circumferential forces

Figure 4.25 shows the influences of the coefficient of friction on circumferential force of roller. The circumferential force increased as the coefficient of friction increased. Ideally, the circumferential force should be close to zero in spinning process because the rollers rotate freely while making contact with the tube. However, in the simulation, the rotational speed of rollers was prescribed according to the assumption of zero relative tangential speed between the rollers and tube. In equation (4.1), r_{roller} should be the radius of contact point of the roller because in reality the contact point was located on the lower part of rounded corner not on the tip. However, the contact point changed with respect to time and was difficult to predict in advance so, for simplicity, the r_{roller} was set as a fixed value, the radius of the tip of roller in the simulation. Therefore, relative tangential speed between the rollers and tube at contact point was not equal to zero. Furthermore, the circumference of tube was discretized into polygonal mesh so the rolling between the tube and the roller was not smooth. In conclusion, it was reasonable that the circumferential force of the roller increased with increasing coefficient of friction.

In summary, the influences of coefficient of friction were significant on twisting angle of the spun tube and circumferential force of roller; by contrast, the influences of coefficient of friction were insignificant on thickness distribution and outer contour of the tube.

4.7 Influence of simulated results using predicted flow stresses

In chapter 2, a hyperbolic-sine Arrhenius-type model was used to predict the flow stresses at various high temperatures and strain rates. Although the accuracy of the prediction was still not good enough, the simulation was executed to discuss the influence of the predicted flow stresses and to verify the usability of this prediction. Similarly, only first four steps of spinning were carried out in these simulations to avoid the mesh distortion problem.

Figure 4.26 and Figure 4.27 show the influences of simulated results using predicted flow stresses on thickness and outer contour of the tubes, respectively. The simulated results using predicted flow stresses were close to those using original flow stresses on both thickness and outer contour of the tube. Therefore, in the simulation, small error of describing flow stresses using a hyperbolic-sine Arrhenius-type model did not affect the dimensional results of neck-spinning process of the tube at elevated temperatures.

Figure 4.28 shows the roller reaction forces in radial, circumferential, and axial directions. Three components of roller reaction force in the simulation using predicted flow stresses were all slightly larger than that using original flow stresses. From Figure 3.8, it could be found that the forming temperatures were approximately 800℃ in most region of the tube during first four steps; moreover, as shown in Figure 2.19, the predicted flow stresses were higher than original stresses at 800℃. Therefore, the roller reaction forces in the simulation using predicted flow stress were larger than that using original flow stresses.

The influence of simulated results using predicted flow stresses was insignificant; therefore, the accuracy of the prediction using Arrhenius-type model was acceptable for the simulation of tube neck-spinning process at elevated temperatures.
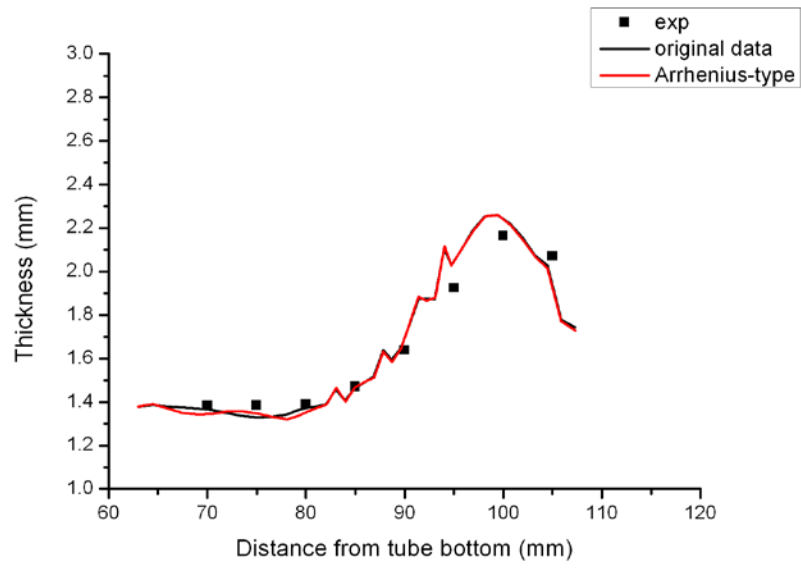
Figure 4.26 The influence of predicted flow stresses on thickness distribution
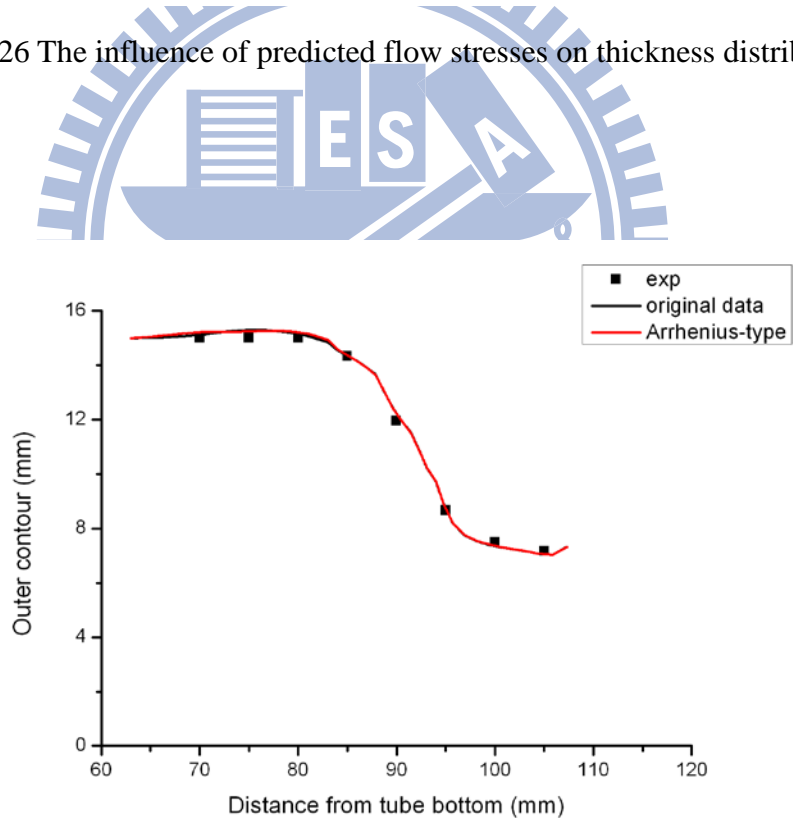
Figure 4.27 The influence of predicted flow stresses on outer contour
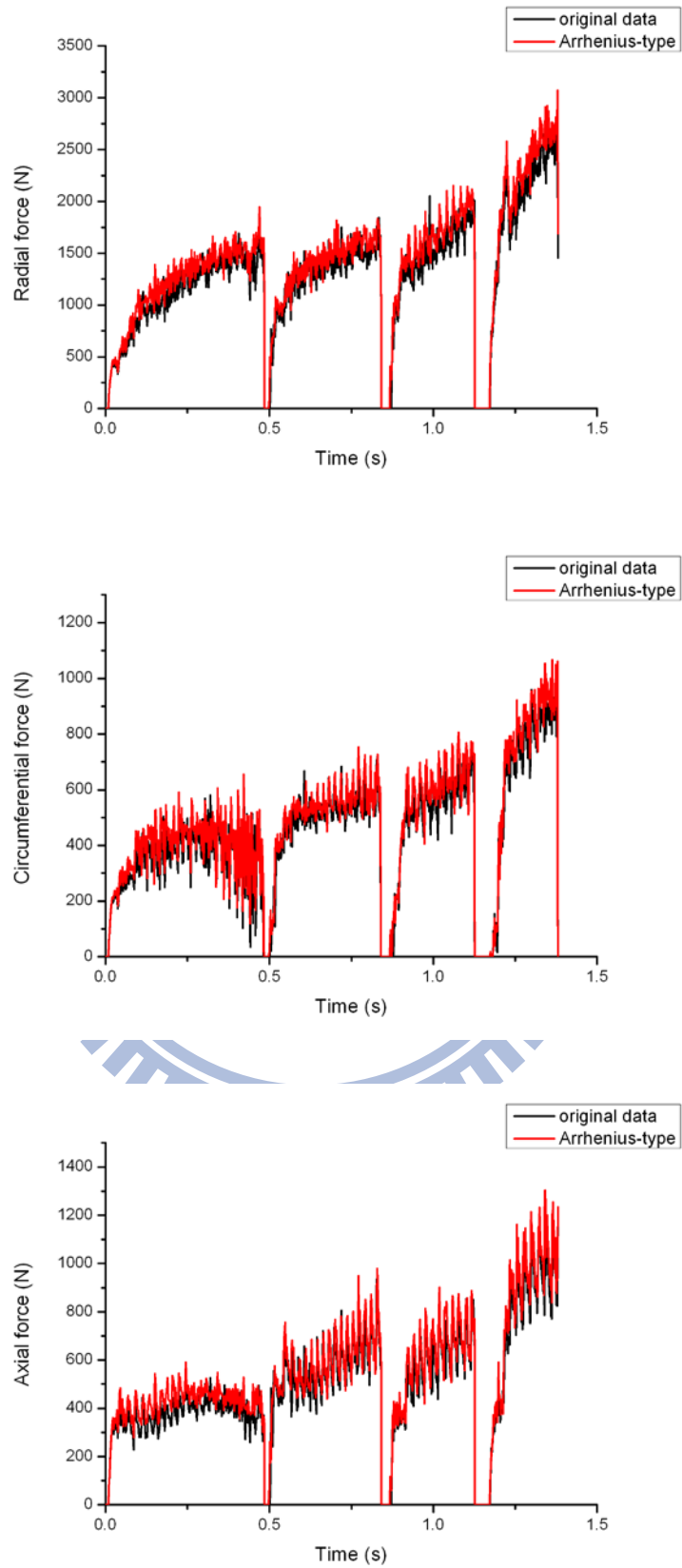
Figure 4.28 The influence of predicted flow stresses on roller reaction forces

4.8 Summary

By incorporating with the flow stresses, obtained at high temperatures and various strain rates, and measured temperature histories of the tube in the experiment, the finite element model for neck-spinning process of the tubes at elevated temperatures was established. The remeshing technique was necessary to diminish the severely distorted meshes and to prevent large numerical errors during the last two steps of spinning. The experimental and simulated results on the thickness distribution and outer contour of the spun tube were discussed to verify the finite element model. Regarding the experimental and simulation results of the thickness distribution and outer contour of the spun tube, the average deviations between the simulation and experiment during the final step were 8.94% in thickness and 1.40% in outer contour. The simulation results corresponded well with those derived from the experiment. Finally, the influences of coefficient of friction and the simulation using predicted flow stresses were discussed.
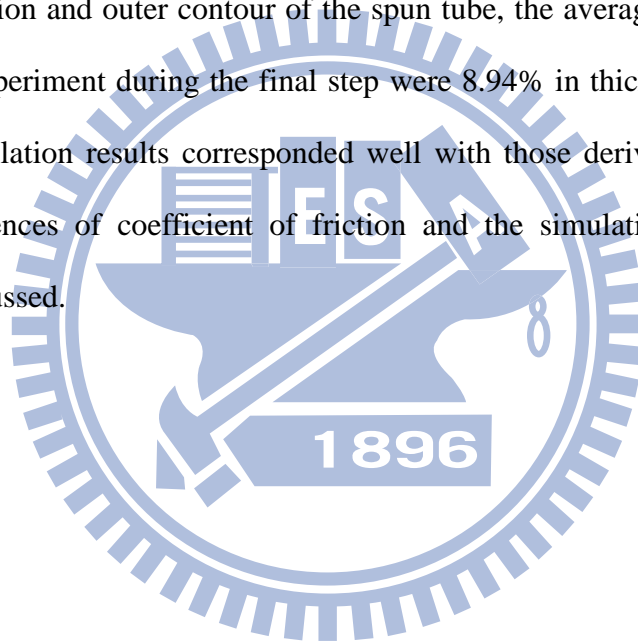
CHAPTER 5 THE INFLUENCES OF PROCESS PARAMETERS OF TUBE NECK-SPINNING

Via experiments of neck-spinning process, the finite element model for tube neck-spinning at elevated temperatures was verified; therefore, the finite element model can be used to investigate the influences of process parameters. Two of most important process parameters in the tube neck-spinning process are the roller feeding pitch and the roller path. In this chapter, the influences of roller feeding pitch were discussed, including wall thickness, outer contour, roundness of tube, and roller forces. Furthermore, the influence of roller forming path on the uniformity of thickness distribution of the tube was also discussed.

5.1 The influence of roller feeding pitch

Roller feeding pitch is one of the most important process parameters in all spinning processes, and it highly affects the production efficiency. Roller feeding pitch is defined as the ratio of roller feeding speed to rotational speed of the spindle. In general, the roller feeding pitch is more representative than roller feeding speed because the brushed contact region between the tube and the roller is determined by the roller feeding pitch. In this study, the original rotational speed of the spindle was 1800 rpm, and the original roller feeding speed was 1600 mm/min so that the roller feeding pitch was 0.8889 mm/rev.

To investigate the influence of roller feeding pitch, various proportions (0.5, 2, 3, and 4) of original roller feeding pitch were tested in the simulations while rotational speed of the spindle was fixed at 1800 rpm. Figure 5.1 shows the schema of brushed contact region between the tube and the roller at various scaling factor of original roller feeding pitch. Furthermore, in order to avoid the mesh distortion problem, only first four steps of spinning were carried out in these simulations.
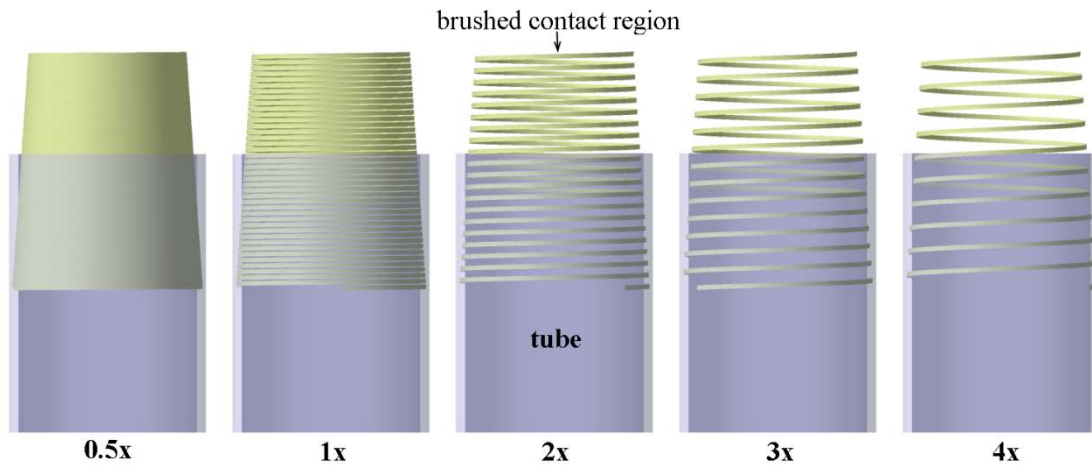
Figure 5.1 Schema of brushed contact region between the tube and the roller at various

proportions of original roller feeding pitch
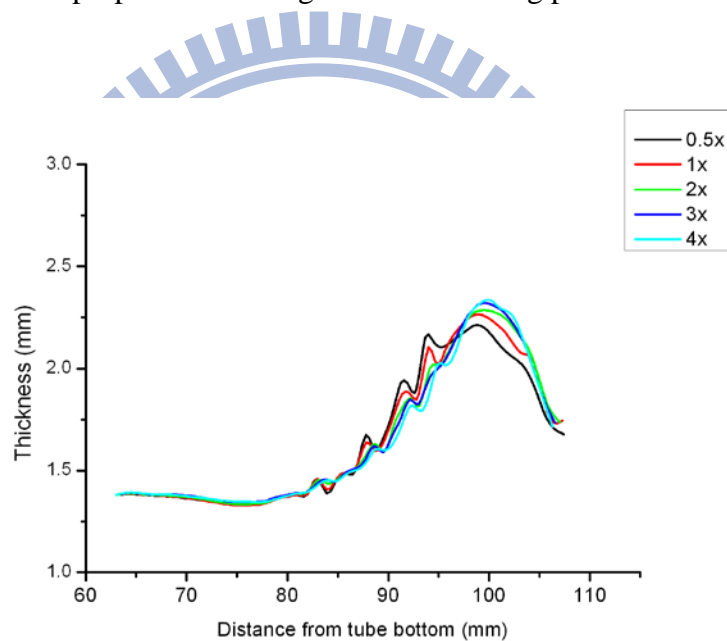
Figure 5.2 The influences of roller feeding pitch on thickness distribution

Figure 5.2 shows the influence of roller forming pitch on thickness distribution of the tube. The thickness at the region of small bulges, which were occurred at the end of each roller forming paths, increased as the roller forming pitch decreased. The small bulges were formed from the build-up of material by rollers; therefore, the smaller roller feeding pitch caused more build-up of material at the end of each roller forming paths so the thickness at small bulges were thicker. Figure 5.3 shows the influence of roller feeding pitch on outer

contour of the tube, and the simulated results were close to each other. The influence of roller feeding pitch on outer contour of the tube was insignificant.
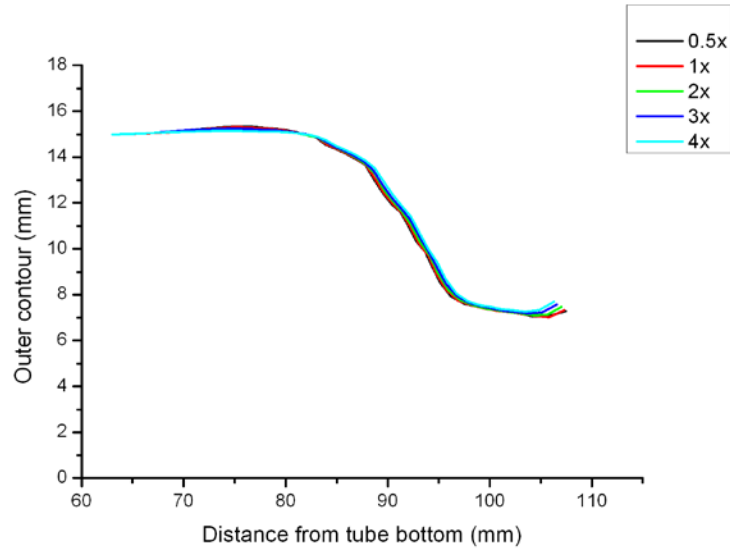
Figure 5.3 The influences of roller feeding pitch on outer contour
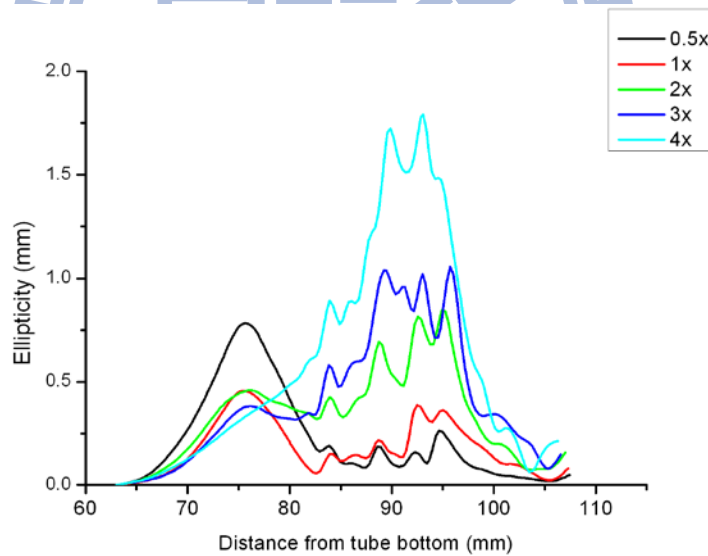
Figure 5.4 The influences of roller feeding pitch on ellipticity

The roundness is another important result affecting the quality of the spun tube. Two estimates are used to indicate the roundness of the spin tube. They are the radius deviation and the ellipticity. The radius deviation is defined as the standard deviation of the outer radius at the same cross section of the tube. The ellipticity is defined as the difference between the

maximum and minimum radius at the same cross section of the tube [15]. Figure 5.4 and Figure 5.5 show the influences of roller feeding pitch on radius deviation and ellipticity, respectively. In the large deformation zone, i.e. the distance from tube bottom is larger than 82 mm, both of radius deviation and ellipticity increased as the roller feeding pitch increased at most region of the tube. Therefore, the roundness of the spun was worse with increased roller feeding pitch.
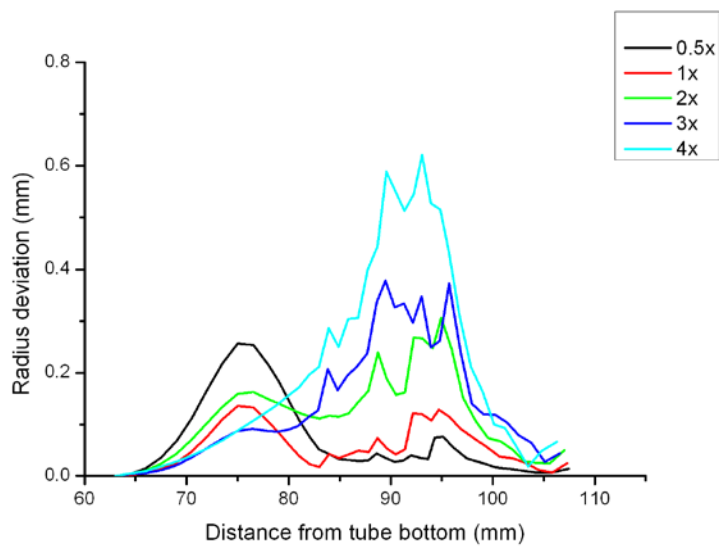
Figure 5.5 The influences of roller feeding pitch on radius deviation

Figure 5.6 shows the influences of roller feeding pitch on roller reaction forces in radial, circumferential, and axial directions. The roller reaction forces in radial and axial directions increased as the roller feeding pitch increased because the strain rates of deformation increased simultaneously as the roller feeding pitch increased and the flow stresses increased as strain rates increased. The influence of roller feeding pitch on circumferential roller reaction force was insignificant because the rotational speed of the spindle was constant in these simulations.
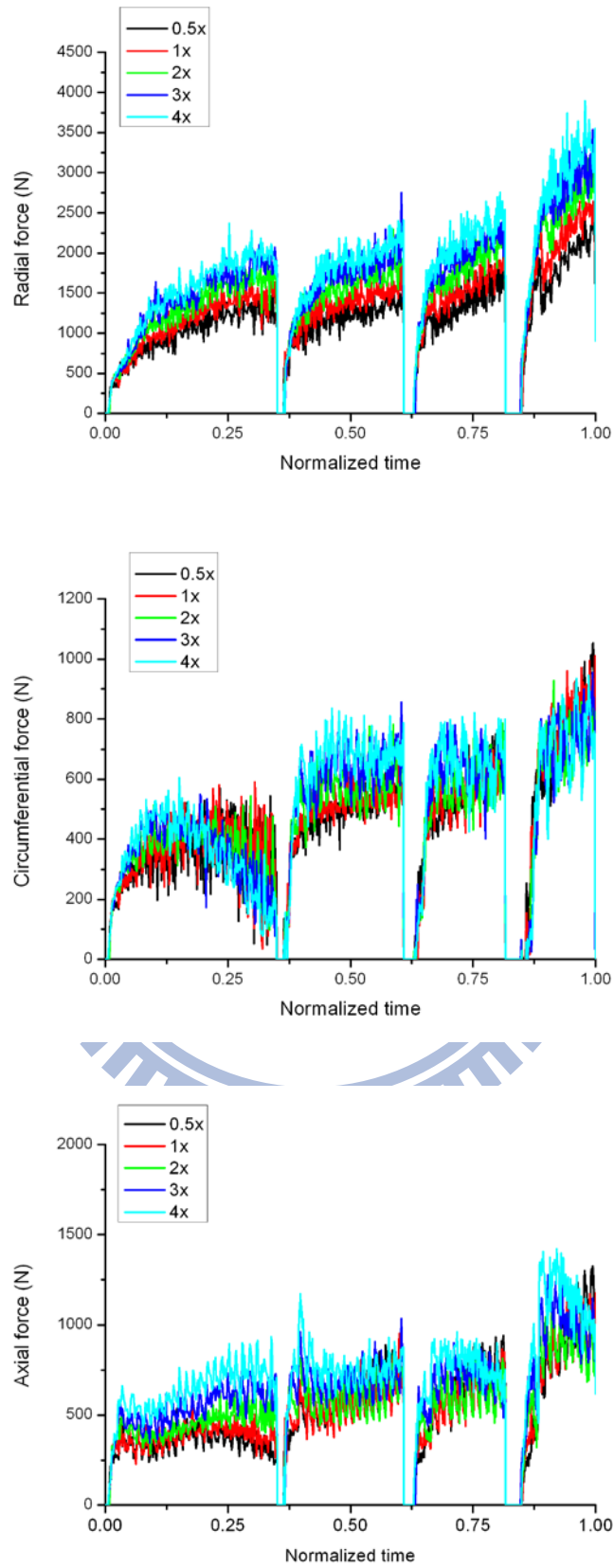
Figure 5.6 The influences of roller feeding pitch on roller reaction forces

Increasing the roller feeding pitch was a practice to increase the production efficiency; however, some defects came with the increased roller feeding pitch. First, the thickness distribution of the spun tube was slightly affected by the roller feeding pitch. Then the roundness of the spun tube got worse with the increment of roller feeding pitch. Finally, the force capacity of the spinning machine should be higher as the roller feeding pitch increased. The above conclusions corresponded well with the experiments from industrial practices.

5.2 The influence of roller forming path

The roller forming path is another important process parameter in spinning processes. In neck-spinning process, the wall thickness distribution of the spun tube was controlled by the roller forming path. In industrial practice, an uneven surface forms on the tube surface if the thickness distribution of the tube is not uniform after the neck-spinning process at elevated temperatures. This is because different thicknesses result in different contractions during the cooling stage. The quality of the spun tube is improved when the thickness distribution is more uniform.

In the first four steps of Figure 3.11, the thickness increased as the spinning process increased, especially at the top of the tube. This occurred because the roller forming paths of the first four steps were all directed from the top of the tube to the bottom. When the forming path is directed from top to bottom, the length of the tube is restricted to elongate so the material flows along a radial direction and the thickness increases. In addition, the forming paths were straight and parallel, so that the maximal radius reduction, which was corresponded to the maximal thickness increase, of each step was all at the top of the tube. Therefore, the thickness distribution is more uniform if the roller forming path is curved and the forming direction reverses between each step.

The first four steps involved rough forming and most of the deformation process was completed during these steps. The final two steps were used to form the designed shape

71

precisely. The influences of the final two steps on the thickness distribution are minute; therefore, the first four forming paths were redesigned to form the tube with more uniform thickness distribution. Figure 5.7 shows the first four steps of new roller forming paths. The simplest curve, an arc, was used as the first three steps. After the first three steps of spinning, the bell mouth occurred at the top of tube; therefore, the fourth step of new roller forming path was composed of two straight lines to diminish the bell mouth to compact the original fifth step of roller forming path.
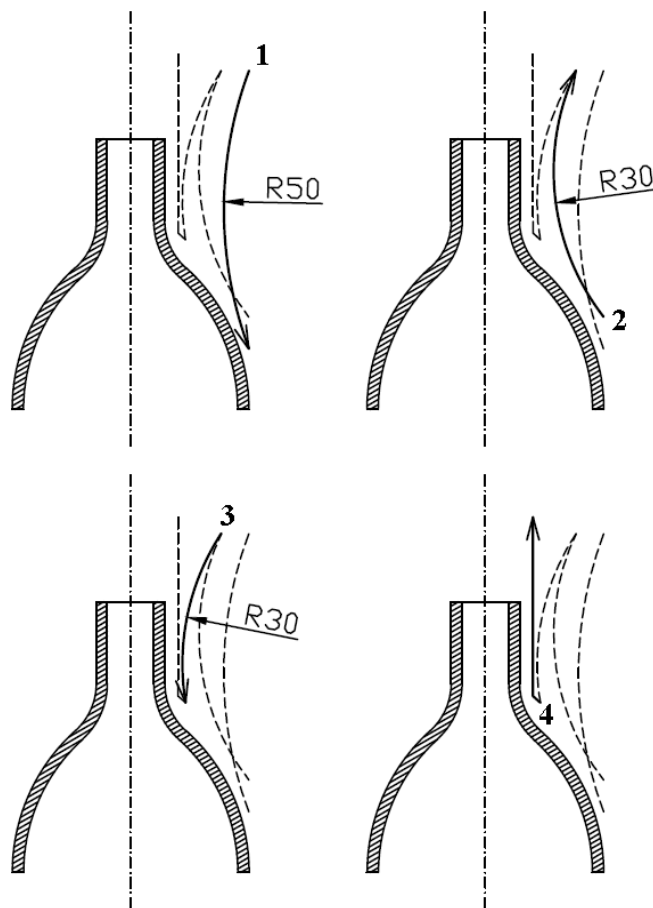
Figure 5.7 Schema of new roller forming paths

Figure 5.8 Six steps of spun tubes using new roller forming paths
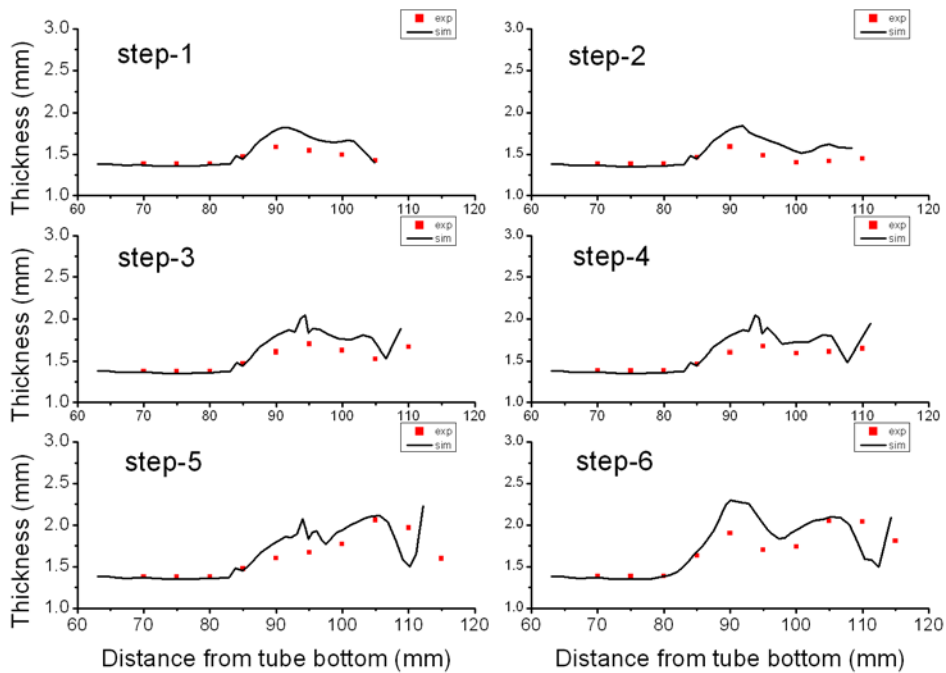
Figure 5.9 Comparison between experimental and simulated results for the thickness of the

tube using new roller forming paths

The new roller forming paths were used in both experiment and finite element simulation. Figure 5.8 shows the results of neck-spinning process using new roller forming path after each of the six steps. An obvious bell-mouth occurred at the top the tube at each of first three steps. Figure 5.9 shows the comparison of thickness distribution of the tube between the simulated and experimental results using new roller forming paths. The deviations between experimental and simulated results for the thickness of the tube were listed in Table 5.1. Regarding thickness, the average deviations from the first to the sixth step between the simulation and experiment were 5.14%, 7.18%, 5.71%, 6.35%, 7.00%, and 8.67%, respectively. The simulated thickness distribution corresponded well with those of the experiment.

Table 5.1 Deviations between experimental and simulated results for the thickness of the tube using new roller forming paths (unit: %)

Position	Step1	Step2	Step3	Step4	Step5	Step6
70	0.74	1.21	0.74	1.38	1.17	1.38
75	1.68	2.24	1.78	2.32	2.13	2.36
80	0.83	1.88	1.08	1.88	1.59	0.45
85	1.38	1.04	1.50	1.09	0.98	2.96
90	13.08	12.87	12.09	12.16	11.97	20.22
95	11.03	14.05	8.42	10.15	10.09	18.53
100	10.60	9.68	7.97	8.07	9.41	11.44
105	1.74	14.45	12.07	11.78	2.34	2.07
110	x	x	x	8.29	23.35	18.64
Average	5.14	7.18	5.71	6.35	7.00	8.67
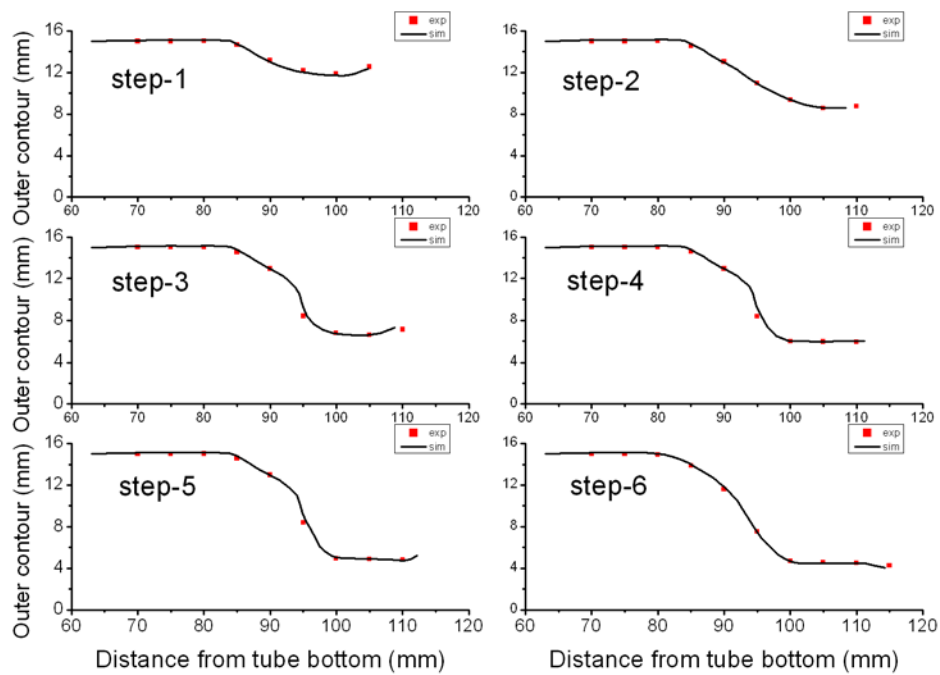
Figure 5.10 Comparison between experimental and simulated results for the outer contour
of the tube using new roller forming paths

Figure 5.10 shows the comparison of outer contour of the tube between the simulated and experimental results using new roller forming paths. The deviations between experimental and simulated results for the thickness of the tube were listed in Table 5.2. Regarding the outer contour, the average deviations from the first to the sixth step between the simulation and experiment were 1.00%, 0.67%, 1.80%, 1.76%, 1.89%, and 1.00%, respectively; hence, the simulated outer contour corresponded accurately with the experimental results. The accuracy of the finite element model for neck-spinning process at elevated temperatures was verified again.

Table 5.2 Deviations between experimental and simulated results for outer contour of the

tube using new roller forming paths (unit: %)

Position	Step1	Step2	Step3	Step4	Step5	Step6
70	0.48	0.63	0.67	0.66	0.68	0.62
75	0.75	0.97	0.99	0.98	1.00	0.91
80	0.64	0.94	0.95	0.93	0.97	0.85
85	0.44	1.27	1.40	1.27	1.24	0.83
90	1.08	0.64	0.11	0.21	0.20	2.16
95	1.50	0.25	9.69	9.38	8.98	0.78
100	1.54	0.05	0.53	0.74	2.09	0.11
105	1.54	0.65	0.08	0.04	0.56	0.98
110	x	x	x	1.62	1.25	1.73
Average	1.00	0.67	1.80	1.76	1.89	1.00

Figure 5.11 shows the influence of roller forming paths on the thickness distribution of the experimental spun tube after each step. The uniformity of thickness distribution of the tube formed by new roller forming paths was better than that of the tube formed by original roller forming paths after the fourth step of spinning process. Although the final two steps were unchanged, the thickness distribution of the tube was still more uniform. Furthermore, the total length of the tube formed by new roller forming paths was longer than that of the tube formed by original roller forming paths, so that the initial length of the tube for the neck-spinning using new roller forming paths could be reduced. Material-saving was another advantage of the spun tube with uniform thickness distribution.
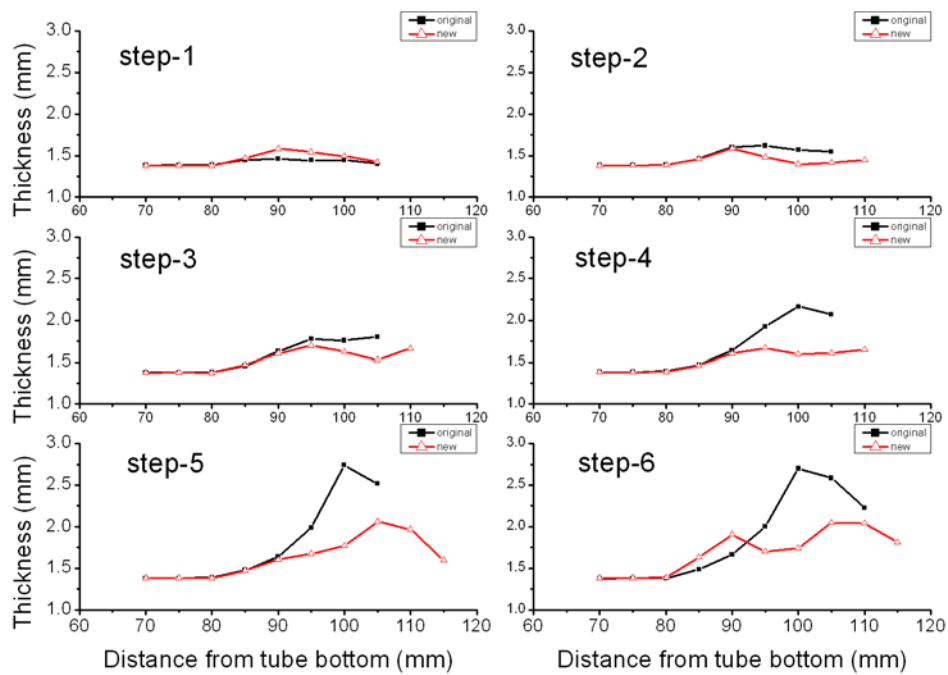
Figure 5.11 The influences of roller forming paths on thickness of experimental spun tube

5.3 Summary

The verified finite element model for tube neck-spinning process at elevated temperatures was used to investigate the influences of two process parameters: the roller feeding pitch and the roller forming path. First, the roundness of the spun tube became worse and the roller reaction forces increased as the roller feeding pitch increased. Finally, for the roller forming path, the thickness distribution of the spun tube formed by curved paths was found to be more uniform than that formed by the original design.

CHAPTER 6 CONCLUSIONS AND FUTURE WORKS

This chapter summarizes the important conclusions of this study on tube neck-spinning process at elevated temperatures. Future research trends of tube neck-spinning process are also outlined.

6.1 Conclusions

With advantages of a high material usage rate, fewer production stages, and flexibility in manufacturing, metal spinning process has been widely used in various applications. In this study, neck-spinning process was applied to form the neck part of high pressure tube ends at elevated temperatures. A comprehensive finite element model incorporating the material properties with strain rate effect was constructed and verified by experiments of tube neck-spinning process. The following summary concludes this study:

1. The accuracy of material properties is crucial for finite element analysis on tube neck-spinning process at elevated temperatures; moreover, the material properties are sensitive to strain rates at hot working process. Therefore, to construct a comprehensive finite element model, the material tests should be performed over a wide range of strains, temperatures, and strain rates. This study performed isothermal hot compression tests at three temperatures (873, 1073, and 1273 K) and six strain rates (0.001, 0.01, 0.1, 1, 10 and 50 s^{-1}) with a maximum strain of 0.8.

2. With comparison of experimental and predicted flow stresses, the Arrhenius-type constitutive model was found to be accurate and suitable for predicting the flow stresses of AISI 1020 steel over a range of strains (0.05-0.8), temperatures (873-1273 K), and strain rates (0.001-50 s^{-1}).

3. From temperature measurement experiment of neck-spinning process, the temperature change of the tube was significant during the process so the temperature effect should be included in the finite element simulation. The local increasing temperature was found as a result of plastic work in the period of forming steps.

4. The remeshing technique was necessary to diminish the severely distorted meshes and to prevent large numerical errors in finite element simulation on tube neck-spinning process at elevated temperatures.

5. Regarding the experimental and simulation results of the thickness distribution and outer contour of the spun tube, the average deviations between the simulation and experiment during the final step were 8.94% in thickness and 1.40% in outer contour. The simulation results corresponded well with those derived from the experiment.

6. Increasing the roller feeding pitch was a practice to increase the production efficiency; however, the roundness of the spun tube became worse and the roller reaction forces increased as the roller feeding pitch increased.

7. To prevent the uneven surface occurred on the spun tube surface, the thickness distribution of the spun tube should be more uniform. In this study, the thickness distribution of the spun tube formed by curved paths was found to be more uniform than that of the tube formed by straight paths.

6.2 Future works

As concluded above, a comprehensive finite element analysis on tube neck-spinning process at elevated temperatures was established in this study. However, the following topics require further study.

1. The tubes and compressive test specimens used in this study were manufactured from rod steel; however, raw material in current industrial practice is sheet steel. Therefore, in order to analyze the tube neck-spinning used in industries, the method of tensile test under high strain rates and high temperatures should be further studied and the work hardening effect of deep drawing process should be included in the finite element simulation.

2. Coupled thermo-mechanical finite element analysis of tube neck-spinning process at elevated temperatures should be further studied and the coupled thermo-mechanical analysis should include the heat transfer between the tube, rollers, and environment, as well as the conversion of plastic work into heat. In this study, the change of temperature distribution of the tube was measured from experiments but that depended on the parameters of the neck-spinning process; therefore, the temperature measurement should be conducted before every finite element simulation with different parameters. For realistic use, coupled thermo-mechanical analysis is necessary because only initial temperature distribution is needed and it can be applied to various cases.

3. Fracture criteria of the material should be further included in the simulation. Decreases in work temperature and increases in forming speed is a practice to minimize the cost in industry; however, the limits of the work temperature and forming speed are determined by the fracture criteria.

4. Future work can consider the combination of finite element analysis and numerical optimization techniques to obtain the optimal roller forming paths to improve the uniformity of thickness distribution of the spun tube.

REFERENCES

[1] C. C. Wong, T. A. Dean, and J. Lin, "A review of spinning, shear forming and flow forming processes", <u>International Journal of Machine Tools & Manufacture</u>, Vol. 43, pp. 1419-1435, 2003.

[2] O. Music, J. M. Allwood, and K. Kawai, "A review of the mechanics of metal spinning", <u>Journal of Materials Processing Technology</u>, Vol. 210, pp. 3-23, 2010.

[3] B. Avitzur, "Metal Forming", <u>Encyclopedia of Physical Science and Technology</u>, Third Edition, Academic Press, New York, 2003.

[4] Y. Jianguo and M. Makoto, "An experimental study on paraxial spinning of one tube end", <u>Journal of Materials Processing Technology</u>, Vol. 128, pp. 324-329, 2002.

[5] Y. Jianguo and M. Makoto, "An experimental study on spinning of taper shape on tube end", <u>Journal of Materials Processing Technology</u>, Vol. 166, pp. 405-410, 2005.

[6] M. J. Roy, R. J. Klassen, and J. T. Wood, "Evolution of plastic strain during a flow forming process", <u>Journal of Materials Processing Technology</u>, Vol. 209, pp. 1018-1025, 2009.

[7] S. Debin, L. Yan, L. Ping, and X. Yi, "Experimental study on process of cold-power spinning of Ti–15–3 alloy", <u>Journal of Materials Processing Technology</u>, Vol. 115, pp. 380-383, 2001.

[8] M. I. Rotarescu, "A theoretical analysis of tube spinning using balls", <u>Journal of Materials Processing Technology</u>, Vol. 54, pp. 224-229, 1995.

[9] J. W. Park, Y. H. Kim, and W. B. Bae, "Analysis of tube-spinning processes by the upper-bound stream-function method", <u>Journal of Materials Processing Technology</u>, Vol. 66, pp. 195-203, 1997.

[10] H. R. Molladavoudi and F. Djavanroodi, "Experimental study of thickness reduction

effects on mechanical properties and spinning accuracy of aluminum 7075-O, during flow forming", International Journal of Advanced Manufacturing Technology, Vol. 52, pp. 949-957, 2011.

[11] A. R. Fazeli and M. Ghoreishi, "Statistical analysis of dimensional changes in thermo-mechanical tube-spinning process", International Journal of Advanced Manufacturing Technology, Vol. 52, pp. 597-607, 2011.

[12] S. Hauk, V. H Vazquez, and T. Altan, "Finite element simulation of the flow-splitting-process", Journal of Materials Processing Technology, Vol. 98, pp. 70-80, 2000.

[13] T. Iguchi, A. Yoshitake, T. Irie, and A. Morikawa, "Numerical Simulation and Development of Tube Spinning Process for Exhaust System Components of Motor Vehicles", AIP conference proceedings, Vol. 712, pp. 1077-1082, 2004

[14] F. A. Hua, Y. S. Yang, Y. N. Zhang, M. H. Guo, D. Y. Guo, W. H. Tong, and Z. Q. Hu, "Three-dimensional finite element analysis of tube spinning", Journal of Materials Processing Technology, Vol. 168, pp. 68-74, 2005.

[15] Q.X Xia, Sh. W. Xie, Y. L. Huo, and F. Ruan, "Numerical simulation and experimental research on the multi-pass neck-spinning of non-axisymmetric offset tube", Journal of Materials Processing Technology, Vol. 206, pp. 500-508, 2008.

[16] M. Murata, T. Kuboki, and T. Murai, "Compression spinning of circular magnesium tube using heated roller tool", Journal of Materials Processing Technology, Vol. 162-163, pp. 540-545, 2005.

[17] K. Mori, M. Ishiguro, and Y. Isomura, "Hot shear spinning of cast aluminium alloy parts", Journal of Materials Processing Technology, Vol. 209, pp. 3621-3627, 2009.

[18] H. Yang, L. Huang, and M. Zhan, "Coupled thermo-mechanical FE simulation of hot splitting spinning process of magnesium alloy AZ31", Computational Materials Science, Vol. 47, pp. 857-866, 2010.

[19] Y. C. Lin and X. M. Chen, "A critical review of experimental results and constitutive descriptions for metals and alloys in hot working", <u>Materials & Design</u>, Vol. 32, pp. 1733-1759, 2011.

[20] Y. C. Lin, M. S. Chen, and J. Zhong, "Constitutive modeling for elevated temperature flow behavior of 42CrMo steel", <u>Computational Materials Science</u>, Vol. 42, pp. 470–477, 2008.

[21] D. Samantary, S. Mandal, and A. K. Bhaduri, "A comparative study on Johnson Cook, modified Zerilli–Armstrong and Arrhenius-type constitutive models to predict elevated temperature flow behaviour in modified 9Cr–1Mo steel", <u>Computational Materials Science</u>, Vol. 47, pp. 568-576, 2009.

[22] A. Rusineka, J. A. Rodríguez-Martínezb, and A. Ariasb, "A thermo-viscoplastic constitutive model for FCC metals with application to OFHC copper", <u>International Journal of Mechanical Sciences</u>, Vol. 52, pp. 120-135, 2010.

[23] G. R. Johnson and W. H. Cook, "A constitutive model and data for metals subjected to large strains, high strain rates and high temperatures", Proceedings of the Seventh International Symposium on Ballistic, pp. 541-547, The Hague, The Netherlands, 1983.

[24] W. S. Lee and C. F. Lin, "High-temperature deformation behaviour of Ti6Al4V alloy evaluated by high strain-rate compression tests", <u>Journal of Materials Processing Technology</u>, Vol. 75, pp. 127-136, 1998.

[25] R. Liang and A. S. Khan, "A critical review of experimental results and constitutive models for BCC and FCC metals over a wide range of strain rates and temperatures", <u>International Journal of Plasticity</u>, Vol. 15, pp. 963-980, 1999.

[26] C. M. Sellars and W. J. McTegart, "On the mechanism of hot deformation", <u>Acta Metallurgica</u>, Vol. 14, pp. 1136-1138, 1966.

[27] K. P. Rao and E. B. Hawbolt, "Development of constitutive relationships using compression testing of a medium carbon steel", <u>Journal of Engineering Materials and</u>

Technology, Vol. 114, pp. 116-123, 1992.

[28] C. Zener and J. H. Hollomon, "Effect of strain rate upon plastic flow of steel", Journal of Applied Physics, Vol. 15, pp. 22-32, 1944.

[29] K. P. Rao and E. B. Hawbolt, "Assessment of simple flow-stress relationships using literature data for a range of steels", Journal of Materials Processing Technology, Vol. 29, pp. 15-40, 1992.

[30] K. P. Rao, Y. K. D. V. Prasad, and E. B. Hawbolt, "Hot deformation studies on a low-carbon steel: Part 1 - flow curves and the constitutive relationship", Journal of Materials Processing Technology, Vol. 56, pp. 897-907, 1996

[31] S. Mandal, V. Rakesh, P. V. Sivaprasad, S. Venugopal, and K. V. Kasiviswanathan, "Constitutive equations to predict high temperature flow stress in a Ti-modified austenitic stainless steel", Materials Science and Engineering A, Vol. 500, pp. 114-121, 2009.

[32] D. Samantaray, S. Mandal, and A. K. Bhaduri, "Constitutive analysis to predict high-temperature flow stress in modified 9Cr–1Mo (P91) steel", Materials & Design, Vol. 31, pp. 981-984, 2010.

[33] H. J. McQueen and N. D. Ryan, "Constitutive analysis in hot working", Materials Science and Engineering A, Vol. 322, pp. 43-63, 2002.

[34] http://www.3ds.com/products/simulia/portfolio/abaqus/abaqus-portfolio/abaqusexplicit/

[35] C. C. Wong, A. Danno, K. K. Tong, and M. S. Yong, "Cold rotary forming of thin-wall component from flat-disc blank", Journal of Materials Processing Technology, Vol. 208, pp. 53-62, 2008.

[36] E. M. Mielnik, Metalworking Science and Engineering, McGraw-Hill, New York, 2002.

[37] L. Wang, "Analysis of Material Deformation and Wrinkling Failure in Conventional Metal Spinning Process", Durham University, Ph. D. thesis, 2012.

[38] Abaqus Analysis User's Manual, Dassault Systemes, 2009.

[39] S. Kobayashi, S. Oh, T. Altan, <u>Metal Forming and the Finite Element Method</u>, Oxford University Press, New York, 1989.

[40] M. S. Mohebbi and A. Akbarzadeh, "Experimental study and FEM analysis of redundant strains on flow forming of tubes", <u>Journal of Materials Processing Technology</u>, Vol. 210, pp. 389-395, 2010.